Sloshing instability and electrolyte layer rupture in liquid metal batteries

Weber, N.; Beckstein, P.; Herreman, W.; Horstmann, G. M.; Nore, C.; Stefani, F.; Weier, T.;

Originally published:

May 2017

Physics of Fluids 29(2017)5, 054101

DOI: https://doi.org/10.1063/1.4982900

Sloshing instability and electrolyte layer rupture in liquid metal batteries

Norbert Weber,[a] Pascal Beckstein,[a] Wietze Herreman,[b] Gerrit Maik Horstmann,[a] Caroline Nore,[b] Frank Stefani,[a] and Tom Weier[a]

(Dated: 12 December 2016)

Liquid metal batteries (LMBs) are discussed today as a cheap grid scale energy storage, as required for the deployment of fluctuating renewable energies. Built as a stable density stratification of two liquid metals separated by a thin molten salt layer, LMBs are susceptible to short-circuit by fluid flows. Using direct numerical simulation, we study a sloshing long wave interface instability in cylindrical cells, which is already known from aluminium reduction cells. After characterising the instability mechanism, we investigate the influence of cell current, layer thickness, density, viscosity, conductivity and magnetic background field. Finally we study the shape of the interface and give a dimensionless parameter for the onset of sloshing as well as for the short-circuit.

PACS numbers: 47.11.Df 47.20.-k 52.30.Cv 47.35.Tv
Keywords: liquid metal battery, magnetohydrodynamics, flow instability, metal pad roll instability, sloshing

[a]Helmholtz-Zentrum Dresden - Rossendorf, Bautzner Landstr. 400, 01328 Dresden, Germany
[b]LIMSI, CNRS, Univ. Paris-Sud, Université Paris-Saclay, Bât 508, rue John von Neumann, Campus Universitaire, F-91405 Orsay, France

I. INTRODUCTION

Liquid metal batteries (LMBs) are among the systems currently discussed for electrochemical energy storage on the grid level. With growing share of renewable and volatile sources, as wind and solar, demand for economic large-scale storage rises. Future energy systems based primarily or even exclusively on renewables can hardly be imagined without adequate storage capacity if electricity demand has to be met independently of the current weather conditions[1] and if grid stability shall be maintained[2].

LMBs consist of a stable density stratification of three liquids: a low density alkaline or earth-alkaline liquid metal on the top, a heavy metal on the bottom and a medium density molten salt mixture sandwiched in between ("differential density cell"[3]; see figure 1a). The operation temperature lies slightly above the highest melting point of the active materials (typically between 275 and 700 °C). Originally, LMBs were investigated as part of thermally regenerative energy conversion systems[4,5], but focus of research later shifted to their application as electricity storage devices[6]. Progress in the field during the 1960s and early 1970s has been reviewed, e.g., by Crouthamel and Recht[7], Cairns et al.[8], Cairns and Shimotake[9,10], and recently by Kim et al.[11]. According to the latter authors, research came to a halt in the 1970s because the low specific energy of LMBs rendered them unattractive for portable applications and "much of the aforementioned research fell into obscurity for the next few decades".

Interest in LMBs has been recently renewed, sparked by the work of Donald Sadoway and his group at MIT[11]. The focus is now on cost-driven development[12] and grid-scale electrochemical storage[11]. Different active material combinations and electrolytes are currently under investigation, ranging from Mg||Sb[13], Ca||Bi[14], Ca||Sb[15], Ca-Mg||Bi[16], Li||Sb-Pb[17] to Na||Pb-Bi[18].

Due to their completely liquid interior, LMBs have attracted the attention of fluid dynamists as well. A number of recent publications are devoted to the problem of the Tayler instability and its circumvention[19–21], to temperature-driven convection[22–24] and electrovortex flows[25–27] in LMBs, and to a simplified model of sloshing in a three layer system[28]. These investigations are motivated on the one hand by the need to prevent a direct contact between anode and cathode melt that could occur if violent motion would develop in the electrode(s) (see figure 1b). On the other hand, mass transport in the lower metal is often

(a) (b)

FIG. 1. Sketch of a liquid metal battery (a) and short-circuit due to a deformation of the electrolyte layer (b).

limiting the cell performance[3,11,13–16,29] calling for enhanced mixing. This could at the same time prevent the sometimes observed accumulation of intermetallic compounds[14,30,31] at the electrode-electrolyte interface.

LMBs are thought to be easily scalable on the cell level due to their simple construction and the self-assembling of the liquid layers. Large cells (in the order of cubic meters[32,33]) are supposed to operate at very high power values[34]. Current densities of up to $13\,\mathrm{A/cm^2}$ were measured for Li||Te cells[9], and less exotic couples as Na||Bi[30] still reach $1\,\mathrm{A/cm^2}$. Together, high current densities and large electrode areas result in strong total currents that are able to generate significant electromagnetic forces. Such forces may give rise to the aforementioned Tayler instability, but may also generate a long wave interfacial instability known from aluminium reduction cells as "sloshing" or "metal pad roll instability". The manifestation of this instability in LMBs is the topic of the paper at hand.

As just mentioned, the metal pad roll instability is well known from the Hall-Héroult process of aluminium production. This two-phase system consists of a stable density stratification of a molten salt mixture (cryolite) floating atop liquid aluminium (figure 2a). A vertical current is applied by graphite current collectors in order to reduce Al_2O_3 (solved in the cryolite) to Al. Although this system works with only two liquid phases, it is quite similar to liquid metal batteries: it operates at about $1\,000\,^\circ\mathrm{C}$, the density difference is only $200\,\mathrm{kg/m^3}$, the salt resistivity is four orders of magnitude higher than the one of the metal, the current density[35] may reach $1\,\mathrm{A/cm^2}$. The main difference is the geometry: aluminium reduction cells are typically rectangular ($4\,\mathrm{x}\,10\,\mathrm{m^2}$) and shallow[36–39].

(a) (b)

FIG. 2. Cross section of an aluminium reduction cell (a) and a liquid metal battery (b) with tilted interface[40,41]. $\boldsymbol{J}$ denotes the total cell current, $\boldsymbol{j}$ the perturbed or compensation current, $\boldsymbol{B}_{0,z}$ a vertical magnetic field and $\boldsymbol{f}$ the resulting Lorentz force.

A possible mechanism explaining the origin of metal pad rolling in aluminium reduction cells was first explained by Sele[40]. We consider a Hall-Héroult cell with a slightly inclined interface between aluminium and cryolite, see figure 2a. The electrolysis current $\boldsymbol{J}$ will take the easy way – this is where the salt layer is thin. A deformation of the interface will thus lead to a perturbed, or compensation current $\boldsymbol{j}$ with a horizontal component. The main idea of Sele's model is an interaction of this *horizontal* current with a *vertical* magnetic field $\boldsymbol{B}_{0,z}$. The latter one originates e.g. from the supply lines; its typical value is between 1 and 10 mT[38]. The cross product of horizontal current and vertical field, the Lorentz force $\boldsymbol{f}$ is pointing towards the observer. Considering only the profile of the cell (figure 2a) it is not so obvious why the Lorentz force will lead to a rotating wave. We illustrate therefore in figure 3 the tilted interface for six different time steps. The perturbed current flows always from a crest (+) of aluminium to a trough (-); the Lorentz force is orthogonal. If we assume the Lorentz force to displace only the crest, we can understand how the rotation develops.

The instability mechanism described above may also be applied to a three layer system of a liquid metal battery[43]. In order to understand certain differences, it is important to know the electric conductivity of the phases: for the salt it is low ($\sim 10^2$ S/m), high for the current collectors ($\sim 10^5$ S/m) and even higher for the liquid metals ($\sim 10^6$ S/m). The strong resistance of the molten salt leads to a purely vertical current in the electrolyte layer (see figure 2a and b). In an aluminium reduction cell, the perturbed current has therefore to close

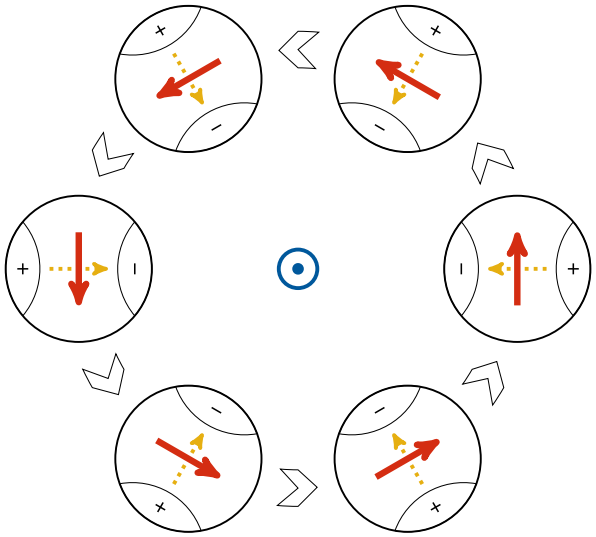

FIG. 3. Top view of the rotation of a tilted interface in a hypotetical aluminium reduction cell with circular shape[42]. The compensation current (yellow) flows from a crest (+) to a trough (-), the Lorentz force (red) is orthogonal to current (yellow) and magnetic field (blue). For the orientation of global current and magnetic field, see figure 2.

in the current collector. In an LMB, it closes already in the upper (liquid) electrode, leading to an additional Lorentz force compared to aluminium reduction cells. This mechanism will be explained in more detail in chapter III A.

Denoting by $\boldsymbol{J}_0$ the current density of an unperturbed cell, the sense of the flow can easily be determined by a simple rule. If $\boldsymbol{J}_0 \cdot \boldsymbol{B}_{0,z} > 0$, the liquid metal layer at the bottom will rotate clockwise; if $\boldsymbol{J}_0 \cdot \boldsymbol{B}_{0,z} < 0$ the flow in the lower metal will be anti-clockwise. This holds for aluminium reduction cells as well as liquid metal batteries. The upper metal layer in LMBs will flow in the opposite direction as the bottom metal. Only the upper interface will deform notably – therefore the wave rotates in the same direction as the upper metal.

The onset criterion of metal pad rolling in (rectangular) aluminium reduction cells was first described by Sele[38,40] as

$$\beta = \frac{J_0 B_{0,z}}{g \Delta\rho} \cdot \frac{l_x}{h_1} \cdot \frac{l_y}{h_2} > \beta_{\mathrm{cr}}, \tag{1}$$

i.e. for stable operation, the dimensionless number β must not exceed a certain critical value[38] in the order of $\beta_{\mathrm{cr}} = 1 \ldots 340$. We will denote by I, J_0 and $B_{0,z}$ the absolute values of cell current, current density and magnetic background field; g, $\Delta\rho = \rho_2 - \rho_1$, h_1, h_2, l_x and l_y refer to the gravity, density difference, the height of the electrolyte and aluminium

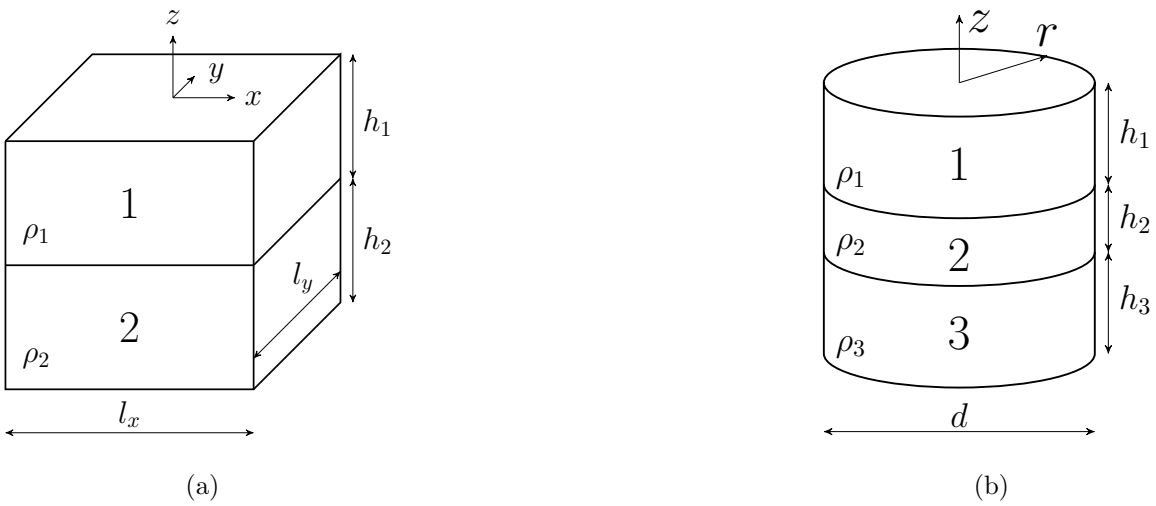

FIG. 4. Sketch of a an aluminium reduction cell (a) and liquid metal battery (b).

layer and the lateral dimensions of the aluminium reduction cell, respectively (see also figure 4a). The first factor in the definition of β is the relation of Lorentz force to gravity force, the two others are aspect ratios and account for the layer thickness.

Using a wave equation approach[44], a formula for β_{cr} was later found as

$$\beta_{\mathrm{cr}} = \pi^2 \left| m^2 \frac{l_y}{l_x} - n^2 \frac{l_x}{l_y} \right| \tag{2}$$

by Bojarevics and Romerio[45]. Here, m and n denote the wave number in x and y of a rectangular cell. Basically, this formula adds the influence of the aspect ratio to the Sele criterion. As a main consequence, square or cylindrical cells will always be unstable, because $l_x = l_y$.

Besides the vertical (and constant) magnetic background field $B_{0,z}$, also spatial gradients of magnetic fields were suspected to lead to instability[46–48]. The derived stability condition for such fields[47] is somehow similar to the one obtained by Bojarevics and Romerio: it is found that cells comprising two waves of equal frequency are always unstable.

A coupling of two modes was further studied by Davidson and Lindsay[41] using a mechanical analog and shallow water approximation. The obtained relation for instability is

$$\frac{J_0 B_{0,z}}{\rho_1 h_2 + \rho_2 h_1} > \frac{|\omega_x^2 - \omega_y^2|}{b_1 + b_2}, \tag{3}$$

with ω denoting the frequency of a standing gravity wave with the wave vector pointing in x or y direction, and b_i some coupling parameters for the different Fourier modes. Again,

square and cylindrical cells are always unstable, because the frequency of one wave in x and a second one in y will be the same.

In some recent papers it was further pointed out that not only a magnetic field and the wave coupling, but also the reflection at the walls is an important ingredient for amplifying the instability[38,49].

Another series of articles is dedicated to the Kelvin-Helmholtz instability in aluminium reduction cells[46,50]. It is well known that the flow between two counter-rotating liquid masses is subjected to shear layer (and other) instabilities[51,52]. However, the resulting waves are typically relatively short and therefore strongly dampened by surface tension; they can not explain the long waves observed in aluminium reduction cells. Usually, Kelvin-Helmholtz waves are considered less important for real cells.

Finally, MHD noise, i.e. short-wave perturbations are often observed experimentally. They develop probably by the turbulent flow in the cell, and are less important for the operation of the reduction cell[38,53].

In summary, the interaction of a horizontal current with a magnetic background field $B_{0,z}$, the coupling of two waves and the wave-reflection at the walls are considered as the crucial elements of the sloshing instability in aluminium cells[38,48]. There already exist several shallow water[54,55] and full 3D models[36,56] for an efficient simulation of aluminium reduction cells.

Aluminium production is not only a good example for two phase, but also for three phase systems. A Hoope's cell (used to refine Al) consists of molten pure aluminium and an aluminium copper alloy, separated by a salt electrolyte[57,58]. To our knowledge, no interface instabilities were reported in this system – maybe due to the low current densities ($0.35\,\mathrm{A/cm^2}$) and the thick electrolyte layer ($>8\,\mathrm{cm}$). Nevertheless, the stability of interfaces in three layer systems was already studied in two theoretical articles[28,59]. Sneyd[59] found the relation for instability

$$\frac{J_0 \cdot (\mu_0 J_0)}{g(\rho_3 - \rho_2)} \cdot \frac{h_2 \cosh(k h_2)}{\sinh^2(k h_2)} > \frac{1}{b'}, \tag{4}$$

with μ_0, b', h_2, ρ_3, ρ_2 and k denoting the vacuum permeability, a dimensionless value, the electrolyte layer height, the density of bottom layer and electrolyte and the wave number (see also figure 4b). As he assumed the liquid electrodes to be infinitely high, his critical parameter does unfortunately not account for the aspect ratio of the cell. Although the above equation looks similar to the Sele criterion, it is not comparable: it holds only for the

interaction of a current with its own magnetic field – there is no magnetic background field $B_{0,z}$ present.

Zikanov was the first to investigate the sloshing instability in liquid metal batteries[28]. He used a mechanical analogue as proposed by Davidson and Lindsay[41]. For the onset of a Sele like sloshing instability, and assuming shallow layers, he found the condition

$$\frac{J_0 B_{0,z}}{\rho_1 h_1} + \frac{J_0 B_{0,z}}{\rho_3 h_3} > \left| \frac{\omega_y^2 - \omega_x^2}{2} \right|, \tag{5}$$

which is very similar to equation (3). The thickness of the electrolyte layer does not appear, because Zikanov supposed it to be very thin. Assuming thick layers with an aspect ratio in the order of one, he finds the instability condition

$$c_1 \frac{J_0 B_{0,z} l_x^2}{12 \rho_1 g h_1 h_2} + c_2 \frac{J_0 B_{0,z} l_x^2}{12 \rho_3 g h_2 h_3} > \left| 1 - \frac{\omega_x^2}{\omega_y^2} \right| \tag{6}$$

with c_1 and c_2 denoting two geometrical constants. He further explored the interaction of an *azimuthal* field with a vertical current – similar to Sneyd. He found the instability condition

$$\frac{\mu_0 J_0 r \cdot J_0}{g} \left(\frac{r^3}{48 \rho_1 h_2^2 h_1} + \frac{r^3}{48 \rho_3 h_2^2 h_3} + \frac{r}{16 \rho_1 h_2} - \frac{r}{16 \rho_3 h_2} \right) > 1 \tag{7}$$

with r denoting the radius of a cylindrical cell.

Some of the critical parameters for onset of sloshing (equation 2, 3, 5 and 6) predict cylindrical cells to be always unstable. However, these criteria neglect dissipation by magnetic induction and viscosity as well as the influence of surface tension[46]. Especially induction effects due to a flow in the cell can increase the critical values for the onset of sloshing[60]. Further, $B_{0,z}$ does not only destabilize the cell: at very high values it can even suppress the instabiliy again[61].

In this article we will study only the influence of a vertical magnetic background field $B_{0,z}$. This is another step forward to understand the complex fluid dynamics involved in the operation of liquid metal batteries. A detailed investigation of the interaction of currents with an azimuthal field (equations 4 and 7) will be postponed to future work.

II. MATHEMATICAL MODEL & IMPLEMENTATION

In this chapter we present a three dimensional multiphase model used for the simulation. The main difference of our model compared to others is the way of computing the magnetic

field. It allows simulation with very realistic boundary conditions. The numerical scheme is developed in close analogy to a MHD model for one single phase[62]; the multiphase aspects are in detail explained in the literature[63–65]. Figure 20 shows the general workflow.

The flow in an incompressible, viscous and electrically conducting fluid of several phases is described by the Navier-Stokes equation (NSE)[64]

$$\frac{\partial(\rho \boldsymbol{u})}{\partial t} + \nabla \cdot (\rho \boldsymbol{u}\boldsymbol{u}) = -\nabla p + \nabla \cdot (\rho\nu(\nabla \boldsymbol{u} + (\nabla \boldsymbol{u})^{\intercal})) - \rho g \boldsymbol{e}_z + \boldsymbol{f}_{\mathrm{L}} + \boldsymbol{f}_{\mathrm{st}} \tag{8}$$

and $\nabla \cdot \boldsymbol{u} = 0$, with $\boldsymbol{u}$, t, ρ, p, ν, g, $\boldsymbol{f}_{\mathrm{L}}$ and $\boldsymbol{f}_{\mathrm{st}}$ denoting velocity, time, density, pressure, kinematic viscosity, gravity, Lorentz force and surface tension, respectively. The unit vector $\boldsymbol{e}_z$ is pointing upwards. Introducing a modified pressure $p_{\mathrm{d}} = p + \rho g z$ by adding the hydrostatic pressure, boundary conditions may be formulated easier and numerical errors reduced. We find

$$\nabla p = \nabla p_{\mathrm{d}} - \rho g \boldsymbol{e}_z - g z \nabla \rho. \tag{9}$$

Introducing the electric current density $\boldsymbol{J}$ and magnetic field $\boldsymbol{B}$, the Lorentz force can be expressed as $\boldsymbol{f}_{\mathrm{L}} = \boldsymbol{J} \times \boldsymbol{B}$. The NSE then becomes

$$\begin{aligned} \frac{\partial(\rho \boldsymbol{u})}{\partial t} + \nabla \cdot (\rho \boldsymbol{u}\boldsymbol{u}) = &- \nabla p_{\mathrm{d}} + g z \nabla \rho + \nabla \cdot (\rho\nu(\nabla \boldsymbol{u} + (\nabla \boldsymbol{u})^{\intercal})) \\ &+ \boldsymbol{J} \times \boldsymbol{B} + \boldsymbol{f}_{\mathrm{st}}. \end{aligned} \tag{10}$$

No-slip boundary conditions are applied for velocity and an equivalent Neumann boundary condition for the pressure:

$$\nabla p_{\mathrm{d}} = \boldsymbol{J} \times \boldsymbol{B} + \boldsymbol{f}_{\mathrm{st}} + g z \nabla \rho. \tag{11}$$

Ohms law for moving conductors

$$\boldsymbol{J} = -\sigma \nabla \phi + \sigma(\boldsymbol{u} \times \boldsymbol{B}) - \sigma \frac{\partial \boldsymbol{A}}{\partial t} \tag{12}$$

allows for calculating the full current density in the cell. The current density of the initial state of rest is

$$\boldsymbol{J}_0 = \frac{I}{S} \boldsymbol{e}_z, \tag{13}$$

with $\boldsymbol{A}$, ϕ, σ, I and S denoting the vector potential, electric potential, electric conductivity, cell current and cross section of the cell. We use in our model the quasi-static approximation[21,66,67], and neglect the temporal derivative of the vector potential ($\partial \boldsymbol{A}/\partial t \approx$

0). Demanding charge conservation ($\nabla \cdot \boldsymbol{J} = 0$) and applying the divergence operator to equation (12), we find a Poisson equation for the electric potential

$$\nabla \cdot (\sigma \nabla \phi) = \nabla \cdot (\sigma(\boldsymbol{u} \times \boldsymbol{B})). \tag{14}$$

As no current is flowing through the side walls of the cylinder, we apply there the boundary condition $\nabla\phi \cdot \boldsymbol{n} = 0$ with $\boldsymbol{n}$ denoting the surface normal vector. We force the perturbed current to form closed loops by adjusting the boundary flux of ϕ at top and bottom according to $\boldsymbol{J}_0$:

$$\nabla\phi \cdot \boldsymbol{n} = -\frac{\boldsymbol{J}_0 \cdot \boldsymbol{n}}{\sigma}. \tag{15}$$

While not completely correct, this is a quite reasonable boundary condition, because the current collectors often have a slightly lower conductivity than liquid metals.

In a last step, the magnetic field $\boldsymbol{B}$ is calculated using the perturbed vector potential $\boldsymbol{a}$ and the magnetic field of an infinitely long cylinder

$$\boldsymbol{B}_{0,\varphi} = \frac{\mu_0 I}{2\pi r}\boldsymbol{e}_\varphi \tag{16}$$

as

$$\boldsymbol{B} = \nabla \times \boldsymbol{a} + \boldsymbol{B}_{0,\varphi} + \boldsymbol{B}_{0,z}. \tag{17}$$

In the quasi-stationary limit ($\partial \boldsymbol{A}/\partial t \approx 0$)[67] and using the Coulomb gauge, the vector potential is obtained by solving the Poisson equation

$$0 = \frac{1}{\mu_0}\Delta \boldsymbol{a} + \boldsymbol{J} - \boldsymbol{J}_0 \tag{18}$$

with the boundary conditions obtained by Green's identity[68]

$$\boldsymbol{a}(\boldsymbol{r}) = \frac{\mu_0}{4\pi}\int dV \frac{\boldsymbol{J}(\boldsymbol{r}') - \boldsymbol{J}_0(\boldsymbol{r}')}{|\boldsymbol{r} - \boldsymbol{r}'|}. \tag{19}$$

This integral can be calculated much faster than Biot-Savart's law – this is the reason why we use the vector potential.

The three different phases of the liquid metal battery are modelled using the volume of fluid method. The phase fraction α_i describes the fraction of fluid i in a single cell. It is determined by solving the transport equation[63,64]

$$\frac{\partial \alpha_i}{\partial t} + \nabla \cdot \boldsymbol{u}\alpha_i = 0. \tag{20}$$

All variable fluid properties are then defined by the phase fraction as

$$\rho = \sum_i \alpha_i \rho_i, \qquad \rho\nu = \sum_i \alpha_i \rho_i \nu_i \quad \text{and} \quad \sigma = \sum_i \alpha_i \sigma_i. \tag{21}$$

Note that the conductivity of the mixture can be calculated as a serial or parallel connection of resistances[69]. Both approaches represent extreme cases. The true conductivity of a cell depends on the angle between the interface and the current density. As this is not known, we use the above mentioned simplified parallel circuit. This may lead to a thinning of the electrolyte layer and overestimate onset and short-circuit of the cell. However, as it smoothes the conductivity at the interface, it stabilises the simulation and is therefore the better choice.

The surface tension is modelled using the continuum surface force (CSF) modell by Brackbill[63,64,70], i.e. it is implemented as a volume force $\boldsymbol{f}_{\text{st}} = \sum_i \sum_{j \neq i} \gamma_{ij} \kappa_{ij} \delta_{ij}$, concentrated at the interface. The contact angle at the walls is assumed to be 90 °. The interface tension γ_{ij} between phases i and j is assumed to be a constant. The curvature between phase i and j is given as

$$\kappa_{ij} \approx -\nabla \cdot \frac{\alpha_j \nabla \alpha_i - \alpha_i \nabla \alpha_j}{|\alpha_j \nabla \alpha_i - \alpha_i \nabla \alpha_j|}, \tag{22}$$

the Dirac delta function $\delta_{ij} = \alpha_j \nabla \alpha_i - \alpha_i \nabla \alpha_j$ ensures that the force is applied only near an interface. Finally, we find

$$\boldsymbol{f}_{\text{st}} \approx -\sum_i \sum_{j \neq i} \gamma_{ij} \nabla \cdot \left(\frac{\alpha_j \nabla \alpha_i - \alpha_i \nabla \alpha_j}{|\alpha_j \nabla \alpha_i - \alpha_i \nabla \alpha_j|} \right) (\alpha_j \nabla \alpha_i - \alpha_i \nabla \alpha_j). \tag{23}$$

First order schemes are used for discretisation of the temporal derivative (Euler implicit) and the convection term (upwind); all other schemes are second order accurate. The grid resolution is 50 cells on the diameter, with a maximum aspect ratio of 3 in the electrolyte layer.

III. RESULTS

In order to illustrate metal pad rolling in LMBs, we model a simple cylindrical Mg||Sb cell of diameter $d = 10\,\text{cm}$. The electrolyte used is NaCl-KCl-$MgCl_2$ (30-20-50 mol%)[11,13,32]. If not otherwise stated, we use the dimensions and physical properties of table I; the current density is $1\,\text{A/cm}^2$ and the assumed magnetic background field $B_{0,z} = 10\,\text{mT}$. This high

TABLE I. Physical dimensions and properties of an Mg|NaCl-KCl-$MgCl_2$|Sb cell[11,72,73].

	h	ρ	ν	σ	γ
	cm	kg/m^3	m^2/s	S/m	N/m
top layer (1)	4.5	1577	$6.7 \cdot 10^{-7}$	$3.62 \cdot 10^6$	0.54
electrolyte (2)	1	1715	$6.8 \cdot 10^{-7}$	80	0.09
bottom layer (3)	4.5	6270	$1.96 \cdot 10^{-7}$	$8.66 \cdot 10^5$	0.37

value (approximately 200 times the magnetic field of the earth) is chosen in order to evidence clearly the effect of metal pad rolling. The interface tensions are estimated using the surface tensions as[71]

$$\gamma_{1|2} = \gamma_1 + \gamma_2 - 2.0\sqrt{\gamma_1 \gamma_2}. \tag{24}$$

We find $\gamma_{1|2} = 0.19\,\mathrm{N/m}$, $\gamma_{1|3} = 0.016\,\mathrm{N/m}$ and $\gamma_{2|3} = 0.095\,\mathrm{N/m}$; the indices 1, 2 and 3 are refering to upper electrode, electrolyte and lower electrode, respectively. The capillary length

$$\lambda = \sqrt{\frac{\gamma_{1|2}}{\Delta\rho g}} = 12\,\mathrm{mm} \tag{25}$$

is approximately 10 % of the cell diameter and 100 % of the electrolyte thickness. We expect therefore no big influence of surface tension on the onset of sloshing, but it may be relevant for a localised short-circuit.

In the initial state of the system, both interfaces are flat; gravity, hydrostatic pressure, an axial magnetic field $\boldsymbol{B}_{0,z}$ and a current I from bottom to top are applied.

A. Driving mechanism of the instability

Figure 5 illustrates a typical saturated sloshing instability in an LMB. The blue crest of electrolyte is localy concentrated, has steep flanks and rotates anticlockwise. The trough is vast, flat and smooth. Crest and trough are not symmetric: the crest tries to catch up the trough. The principal flow matches well to the deplacement of the wave crest. The streamlines in the upper metal close directly above the crest, or in a long azimuthal flow.

In order to explain the instability mechanism, we plot several features on a plane indicated by the black line in figure 5. The cell current $\boldsymbol{J}$ concentrates on the pinched side of the electrolyte (figure 6b). Substracting the current of an unperturbed cell ($\boldsymbol{J}_0$), we obtain the

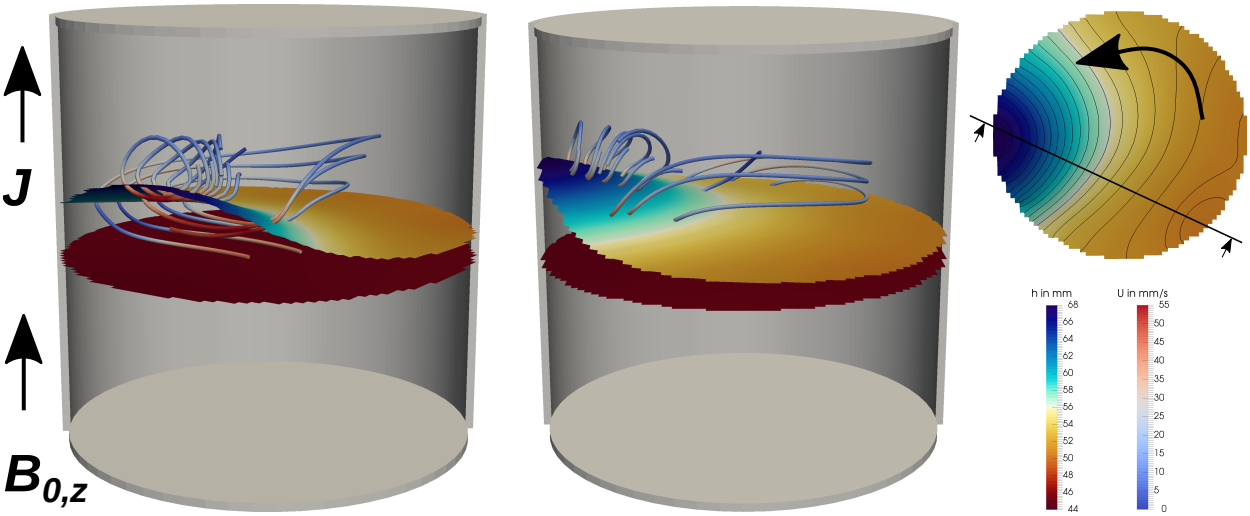

FIG. 5. Streamlines of velocity, surface elevation and direction of rotation for a saturated sloshing instability in a liquid metal battery ($I = 120\,\mathrm{A}$, $B_z = 10\,\mathrm{mT}$, $h_1 = h_3 = 4.5\,\mathrm{cm}$, $h_2 = 1\,\mathrm{cm}$).

compensation current $\boldsymbol{j}$ in figure 6c. This current distribution is not surprising; it strongly resembles the simple model described in the introduction. Please note that we force the perturbed current to close within the cell by applying Neumann boundary conditions for the electric potential.

Applying a constant vertical magnetic field $\boldsymbol{B}_{0,z}$ and denoting the unperturbed magnetic field as $\boldsymbol{B}_{0,\varphi}$ and the perturbed one as $\boldsymbol{b}$, the Lorentz force can be expressed by four relevant

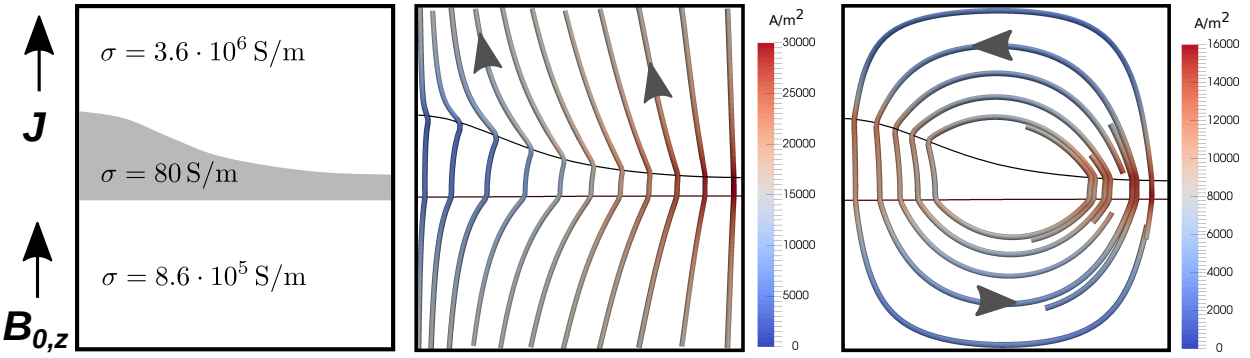

(a) (b) (c)

FIG. 6. Conductivity (a), complete current $\boldsymbol{J}$ (b) and compensation or perturbation current $\boldsymbol{j}$ (c) for a deformed interface between upper metal and electrolyte layer ($I = 120\,\mathrm{A}$, $B_z = 10\,\mathrm{mT}$, $h_1 = h_3 = 4.5\,\mathrm{cm}$, $h_2 = 1\,\mathrm{cm}$). The location of the plane is indicated in figure 5.

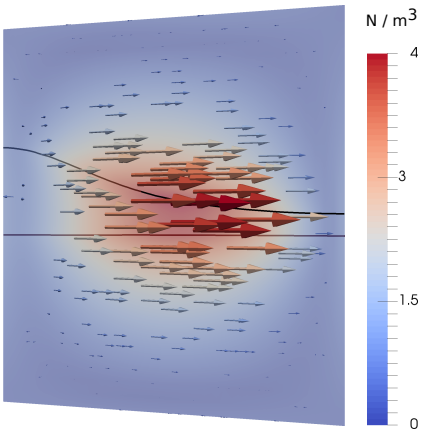

(a) $\boldsymbol{J}_0 \times \boldsymbol{b}$: stabilising

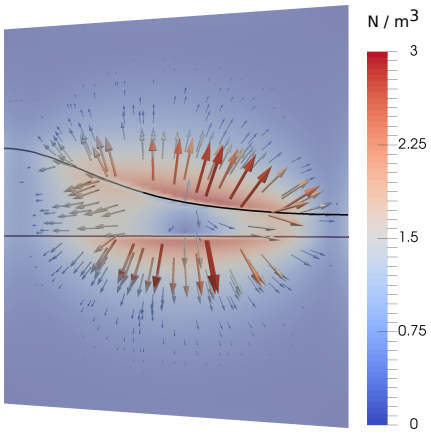

(b) $\boldsymbol{j} \times \boldsymbol{b}$: stabilising

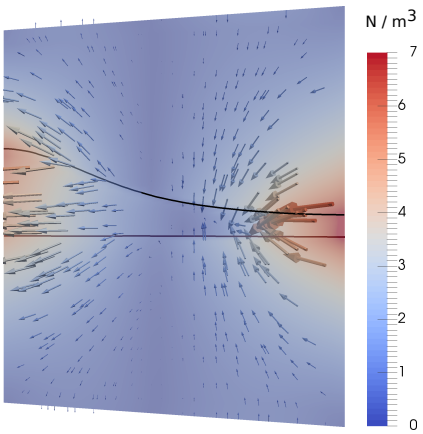

(c) $\boldsymbol{j} \times \boldsymbol{B}_{0,\varphi}$: destabilising

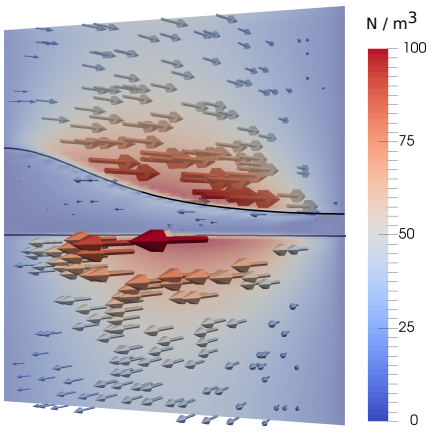

(d) $\boldsymbol{j} \times \boldsymbol{B}_{0,z}$: destabilising

FIG. 7. Different Lorentz forces for a sloshing instability. The prescribed current of $I = 120\,\mathrm{A}$ flows upwards, the background magnetic field $B_{0,z} = 10\,\mathrm{mT}$ points upwards ($h_1 = h_3 = 4.5\,\mathrm{cm}$, $h_2 = 1\,\mathrm{cm}$). The location of the plane is indicated in figure 5.

summands:

$$\boldsymbol{f}_\mathrm{L} = \boldsymbol{J}_0 \times \boldsymbol{b} + \boldsymbol{j} \times \boldsymbol{B}_{0,\varphi} + \boldsymbol{j} \times \boldsymbol{B}_{0,z} + \boldsymbol{j} \times \boldsymbol{b}. \tag{26}$$

Please note that $\boldsymbol{J}_0 \times \boldsymbol{B}_{0,\varphi}$ is a pure gradient and drives no flow; $\boldsymbol{B}_{0,z}$ is parallel to $\boldsymbol{J}_0$.

In figure 7 we illustrate the four relevant force components in the same plane as before. Firstly, we notice that the perturbed magnetic field $\boldsymbol{b}$ always stabilises the interface (figure 7a and b). However, the interaction of a horizontal current and the azimuthal field ($\boldsymbol{j} \times \boldsymbol{B}_{0,\varphi}$) destabilises the electrolyte (figure 7c). This was already suggested by Zikanov[28], but without considering the two damping forces.

Finally, we show in figure 7d the interaction of a horizontal current and $\boldsymbol{B}_{0,z}$. This force

is by far the largest and considered as the main source of the sloshing instability[38]. We observe almost no force in the electrolyte; the upper metal is driven anti-clockwise, the lower clockwise and both forces are equally large. Considering that $\boldsymbol{B}_{0,z}$ points upwards, the observed Lorentz force can already be deduced easily from the current distribution in figure 6c. The force in the upper metal will lead to a rotating flow (figure 5), pushing the crest of electrolyte in front of it. This may explain the rotation of the wave, but not the increase of its amplitude. Indeed, a reflection of the sloshing fluid at the cylinder wall will lead to a deformation of the upper metal-electrolyte interface[49]. This coupling at the walls is assumed to be essential for the instability[38].

B. Characterisation of the instability and parameter studies

In this section we will study the influence of several parameters on the sloshing instability in liquid metal batteries. We simulate the same Mg||Sb cell as in the preceeding case and vary the cell current I, the background field $B_{0,z}$, the heights of the top layer h_1, electrolyte h_2 and bottom metal h_3, as well as the electrolyte conductivity σ_2, the top metal density ρ_1 and the viscosity ν. Note that a change of a layer thickness implies also a change of the cells aspect ratio. We start our simulation with plane interfaces and track the minimal salt layer thickness h_E over time until reaching a saturated state (see figure 8a). The period of rolling

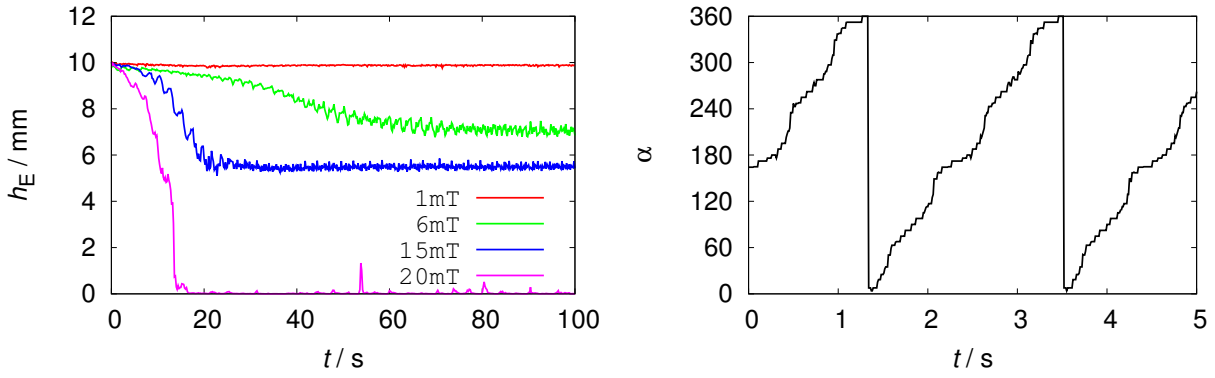

(a) (b)

FIG. 8. Temporal evolution of the minimal salt layer thickness for different background magnetic fields (a), and of the corresponding angle (b) for $B_{0,z} = 6\,\mathrm{mT}$ ($I = 78.5\,\mathrm{A}$, $h_1 = h_3 = 4.5\,\mathrm{cm}$, $h_2 = 1\,\mathrm{cm}$).

(figure 8b) is determined, too. It is expected to deviate only slightly from the period of the gravity wave[38,39]. Further we expect that the natural sloshing frequencies in LMBs can be suitably approximated by wave solutions of two-layer systems due to the high density of the bottom alloy. To check this presumption we deduce dispersion relations of the two-phase and the three-phase system for cylindrical vessels using potential theory. For the angular frequency ω in a two-phase system we receive

$$\omega_{mn}^2 = \frac{(\rho_2 - \rho_1) g \frac{\epsilon_{mn}}{R} + \gamma_{1|2} \left(\frac{\epsilon_{mn}}{R}\right)^3}{\rho_1 \coth(\frac{\epsilon_{mn}}{R} h_1) + \rho_2 \coth(\frac{\epsilon_{mn}}{R} h_2)} \tag{27}$$

where R and g denote the radius and gravitational acceleration. The wave number ϵ_{mn} corresponds to the nth roots of the first derivative $J_m'(\epsilon_{mn}) = 0$ of the mth-order Bessel function of the first kind with valid modes $m = 0, 1, 2, \ldots$ and $n = 1, 2, \ldots$, respectively. Within a three-layer system natural frequencies can be expressed by

$$\omega_{1|2,mn}^2 = \frac{(\rho_2 - \rho_1) g \frac{\epsilon_{mn}}{R} + \gamma_{1|2} \left(\frac{\epsilon_{mn}}{R}\right)^3}{\rho_1 \coth(\frac{\epsilon_{mn}}{R} h_1) + \rho_2 \left(\coth(\frac{\epsilon_{mn}}{R} h_2) + \frac{A_{mn}^2}{A_{mn}^1} \frac{1}{\sinh(\frac{\epsilon_{mn}}{R} h_2)}\right)} \tag{28}$$

$$\omega_{2|3,mn}^2 = \frac{(\rho_3 - \rho_2) g \frac{\epsilon_{mn}}{R} + \gamma_{2|3} \left(\frac{\epsilon_{mn}}{R}\right)^3}{\rho_3 \coth(\frac{\epsilon_{mn}}{R} h_3) + \rho_2 \left(\coth(\frac{\epsilon_{mn}}{R} h_2) + \frac{A_{mn}^1}{A_{mn}^2} \frac{1}{\sinh(\frac{\epsilon_{mn}}{R} h_2)}\right)} \tag{29}$$

with A_{mn}^1 and A_{mn}^2 denoting the amplitudes of the upper and lower interface. The deviation of the frequency ω_{12mn}^2 of the upper surface, which is expected to be mainly excited by the sloshing instability, from the two-layer frequency is only manifested in the term

$$\frac{A_{mn}^2}{A_{mn}^1} \frac{1}{\sinh(\frac{\epsilon_{mn}}{R} h_2)}. \tag{30}$$

Hence, expression (30) can be exploited to analyse the validity of the two-layer approximation. From there, the two-layer relation is suitable if, e.g., the lower amplitude becomes small enough, $A_{mn}^2 \ll 1$, or if the aspect ratio of the electrolyte becomes sufficiently large $h_2/R \gg 1$. In order to be able to calculate the three-layer frequencies the amplitude ratios

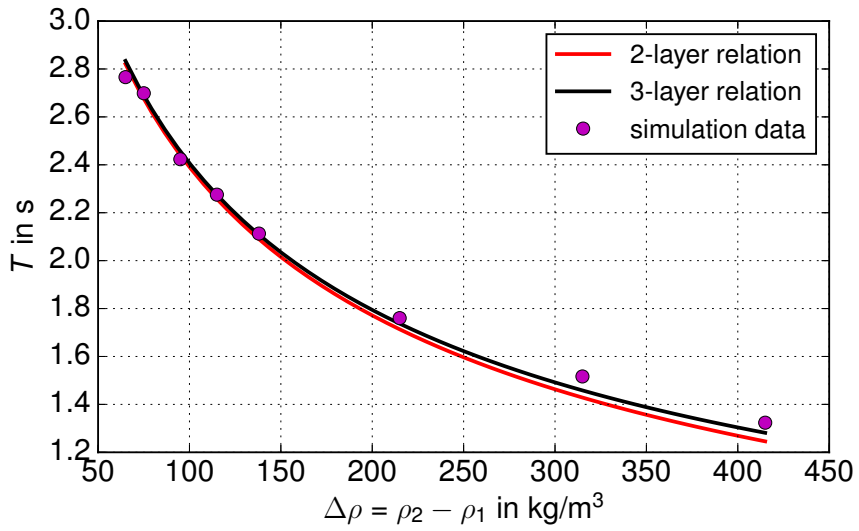

FIG. 9. Theoretical and simulated period of metal pad rolling with changing density ρ_1 ($I = 78.5\,\mathrm{A}$, $B_z = 10\,\mathrm{mT}$, $h_1 = h_3 = 4.5\,\mathrm{cm}$, $h_2 = 1\,\mathrm{cm}$, $\rho_2 = 1715\,\mathrm{kg/m^3}$, $\rho_3 = 6270\,\mathrm{kg/m^3}$).

in both relations (28) and (29) must be eliminated yielding the secular equation

$$a\omega^4 + b\omega^2 - c = 0$$

with

$$\begin{aligned}
a &= \frac{\rho_2^2}{\sinh(\frac{\epsilon_{mn}}{R}h_2)^2} - \left(\rho_2 \coth(\frac{\epsilon_{mn}}{R}h_2) + \rho_3 \coth(\frac{\epsilon_{mn}}{R}h_3)\right) \\
&\quad \times \left(\rho_2 \coth(\frac{\epsilon_{mn}}{R}h_2) + \rho_1 \coth(\frac{\epsilon_{mn}}{R}h_1)\right) \\
b &= \left((\rho_2 - \rho_1)g\frac{\epsilon_{mn}}{R} + +\gamma_{1|2}\left(\frac{\epsilon_{mn}}{R}\right)^3\right)\left(\rho_2 \coth(\frac{\epsilon_{mn}}{R}h_2) + \rho_3 \coth(\frac{\epsilon_{mn}}{R}h_3)\right) \\
&\quad + \left((\rho_3 - \rho_2)g\frac{\epsilon_{mn}}{R} + \gamma_{2|3}\left(\frac{\epsilon_{mn}}{R}\right)^3\right)\left(\rho_2 \coth(\frac{\epsilon_{mn}}{R}h_2) + \rho_1 \coth(\frac{\epsilon_{mn}}{R}h_1)\right) \\
c &= \left((\rho_2 - \rho_1)g\frac{\epsilon_{mn}}{R} + \gamma_{1|2}\left(\frac{\epsilon_{mn}}{R}\right)^3\right)\left((\rho_3 - \rho_2)g\frac{\epsilon_{mn}}{R} + \gamma_{2|3}\left(\frac{\epsilon_{mn}}{R}\right)^3\right).
\end{aligned} \tag{31}$$

For the first mode that has the wave number $\epsilon_{11} = 1.841$ we find the period $T_{1|2} = 2.09\,\mathrm{s}$ with the two-layer formula and $T_{1|2} = 2.11\,\mathrm{s}$ and $T_{2|3} = 0.45\,\mathrm{s}$ with the three-layer formula. The values for the upper interface ($T_{1|2}$) are almost equal for both formulas; the value obtained in the simulation of our standard case is $T_{1|2} = 2.18\,\mathrm{s}$. Figure 9 shows the periods for various simulations with changing density compared to both the theoretical 2-layer (28) and 3-layer (29) formula. While both agree suitably with the numerical data, the three-layer dispersion relation matches slightly better for the large density differences. All in all,

the two-layer relation has been confirmed as a suitable approximation for our liquid battery model. Nevertheless, the dynamics of the lower interface play a certain role for the evolution of short-circuits, as outlined in section III C, and therefore may not be fully neglected.

In a first step of our parameter study we characterize the influence of cell current and magnetic field: both are amplifying the instability. Figure 10a shows the height of the salt layer h_E (divided by its initial height h_{E0}) depending on the cell current. Until 30 A we do not observe any deformation of the interface, the cell is stable. Later on, the electrolyte's minimal height decreases with the current. This behaviour represents a bifurcation. At 170 A we observe a sudden rupture of the interface. Changing the magnetic background field (figure 10b) gives a very similar result – with bifurcation points at 2 and 15 mT.

In a second step we examine the influence of the initial heights of the upper metal and the electrolyte layer. A shallow electrode and/or electrolyte is more unstable – see figure 10c and d. A fully stable cell can not be observed; even very high layers suffer some deformation. However, the short-circuit again appears very suddenly when reaching an electrolyte layer thickness of 7 mm or an aspect ratio of the top layer of 0.2. In real cells, the electrolyte layer is supposed to be between 4 and 10 mm thick; the height of the upper electrode depends on the required capacity of the cell.

In a third step we explore the influence of density and electric conductivity. In figure 10e we show the minimal salt layer thickness depending on the density difference between top metal and salt $\Delta\rho$. As for current and magnetic field, a bifurcation appears at $\Delta\rho = 515\,\mathrm{kg/m^3}$. The cell fails suddenly below of $\Delta\rho = 60\,\mathrm{kg/m^3}$. Note that the density gap between electrolyte and bottom metal is always very high – we never observed a considerable deformation of the lower interface. Decreasing the ratio of electric conductivity (figure 10f) only one bifurcation occurs while no short-circuit can be observed. Real LMBs usually have a conductivity ratio of 10^{-5}. As the interface deformations does not change much for a conductivity ratio between 10^{-6} and 10^{-3}, it might be possible to simulate with a higher conductivity of the salt layer in order to avoid numerical problems.

Finally, we study the influence of viscosity, assuming the same viscosity for all phases. Typical viscosities in the order of $(10^{-7} \ldots 10^{-6}\,\mathrm{m^2/s})$ considerably dampen the instability (figure 11). Viscosity should therefore be included in a dimensionless number describing the sloshing in LMBs.

In order to compare better the influence of the various parameters on metal pad rolling,

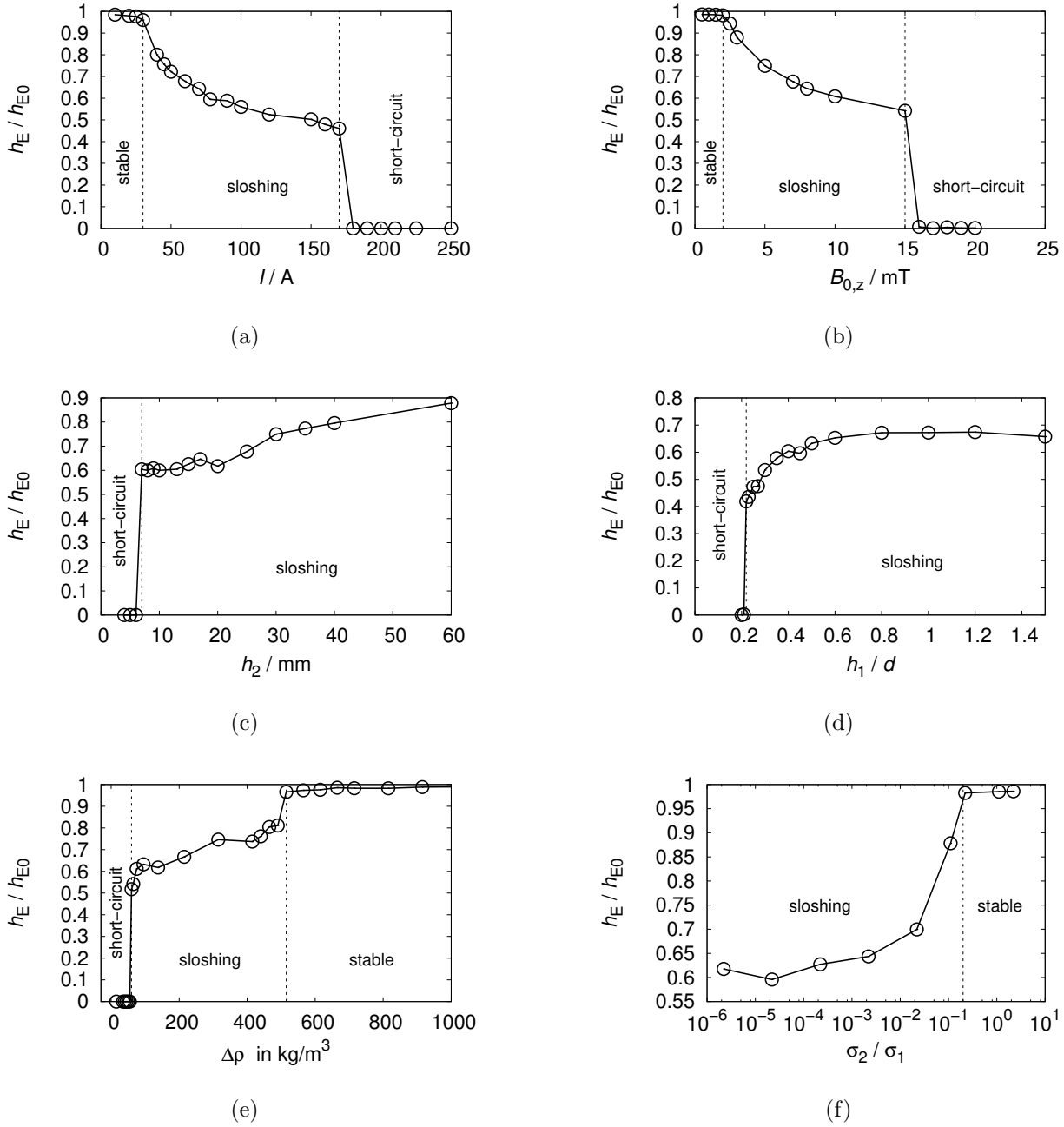

FIG. 10. Minimal relative height of the salt layer depending on the cell current (a), the vertical magnetic background (b), the initial heights of the salt (c) and the upper metal layer (d), the density difference between upper metal and electrolyte (e) and the ratio of salt to upper metal conductivity (f). If not being the variable quantity, the following values are used: $I = 78.5\,\mathrm{A}$, $B_{0,z} = 10\,\mathrm{mT}$, $h_1 = h_3 = 4.5\,\mathrm{cm}$, $h_2 = 1\,\mathrm{cm}$. For the material parameters, see table I.

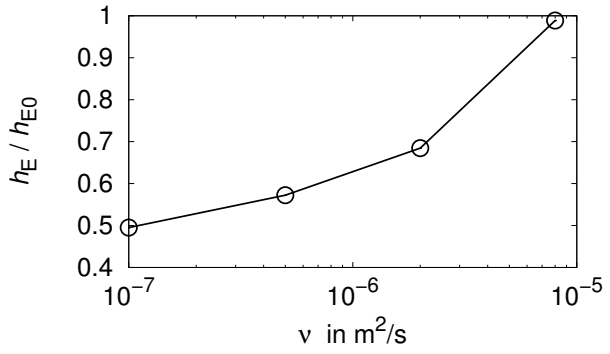

FIG. 11. Minimal relative height of the salt layer for changing viscosity of the fluids. The same viscosity is assumed for all phases ($I = 78.5\,\mathrm{A}$, $B_z = 10\,\mathrm{mT}$, $h_1 = h_3 = 4.5\,\mathrm{cm}$, $h_2 = 1\,\mathrm{cm}$).

we use equations (1), (3), (5) and (6) to define four different dimensionless parameters:

$$\beta_{\mathrm{Sele}} = \frac{I B_{0,z}}{g(\rho_2 - \rho_1) h_1 h_2} \tag{32}$$

$$\beta_{\mathrm{Davidson}} = \frac{J_0 B_{0,z} d}{g(\rho_1 h_2 + \rho_2 h_1)} \tag{33}$$

$$\beta_{\mathrm{Zikanov,\ thin\ layers}} = \frac{J_0 B_{0,z} d}{g \rho_1 h_1} + \frac{J_0 B_{0,z} d}{g \rho_3 h_3} \tag{34}$$

$$\beta_{\mathrm{Zikanov,\ thick\ layers}} = \frac{J_0 B_{0,z} d^2}{12 g \rho_1 h_1 h_2} + \frac{J_0 B_{0,z} d^2}{12 g \rho_3 h_2 h_3} \tag{35}$$

In its original meaning, these parameters describe only the onset, but not the nonlinear part of the instability. While the first and second one were developed for only two phases, the last two should work for three phases of a real LMB. All but the last parameters were developed using the shallow water approximation, i.e. for shallow layers; it is therefore not straightforward to apply them to our cell.

In figures 12 and 13 we illustrate the final height of the salt layer depending on β. The five different curves represent a change of the cell current, magnetic field, initial height of the upper metal or electrolyte and density. In all diagrams we observe a good coincidence of the curves for varying I and $B_{0,z}$. A certain deviation can be explained by the different damping nature of an increasing I or $B_{0,z}$[61].

The curves for changing the height of the anode or electrolyte layer already deviate significantly. For small β especially the anode curve will *not* converge to one, i.e. metal

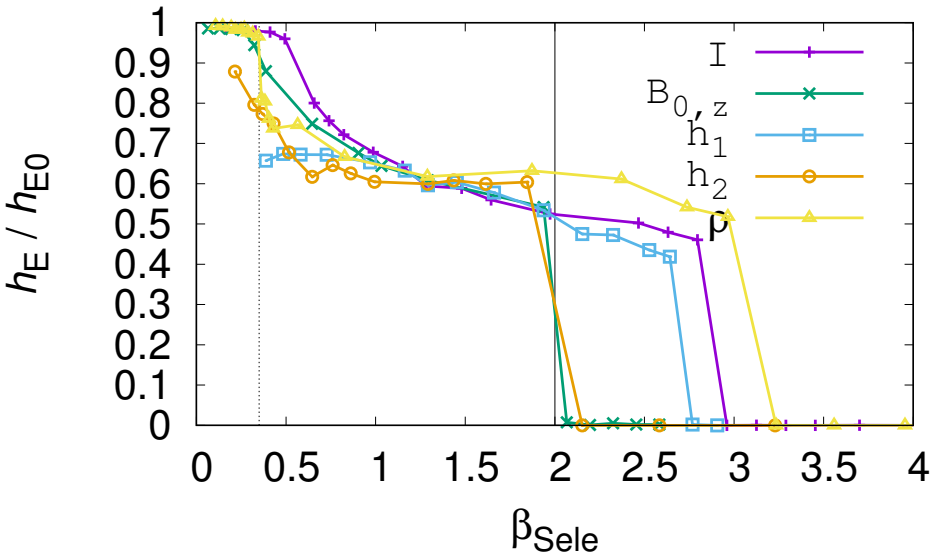

FIG. 12. Remaining minimal salt layer thickness depending on the dimensionless parameter β as defined by Sele[38,40]. The value of the cell current I, the vertical field $B_{0,z}$, the height of upper metal and electrolyte layer h_1 and h_2 as well as the density are varied.

pad rolling can appear in infinitely high cells. None of the dimensionless parameters can correctly describe the onset of metal pad rolling depending on the layer height; this is not surprising as almost all parameters were developed for shallow layers only. However, the region of short circuit still seems to be described quite well, especially by β_{Sele}.

Finally, β_{Davidson} and β_{Zikanov} do not describe the influence of density acceptably, while β_{Sele} yields a good coincidence with the curves for I and $B_{0,z}$. We will therefore focus on the original Sele criterion in the following. At $\beta_{\text{cr}} \approx 0.35$, metal pad rolling appears for the first time; for lower values of β the cell is stable (for our aspect ratio). In contrast to linear stability analysis which suggests that cylindrical cells are always unstable[45] ($\beta_{\text{cr}} = 0$), our result indicate that viscosity, induction and/or surface tension effects can shift the threshold for onset of sloshing.

A second remarkable region in figure 12 is $\beta = 2.0 \ldots 3.2$ – here the cell is short-circuited very suddenly. This happens typically at a remaining salt layer thickness of about 50% of the initial value. It is not clear, whether $\beta > 2$ or a certain salt layer thickness are responsible for the sudden short-circuit.

In summary, the Sele criterion β allows quite well defining the onset of metal pad rolling

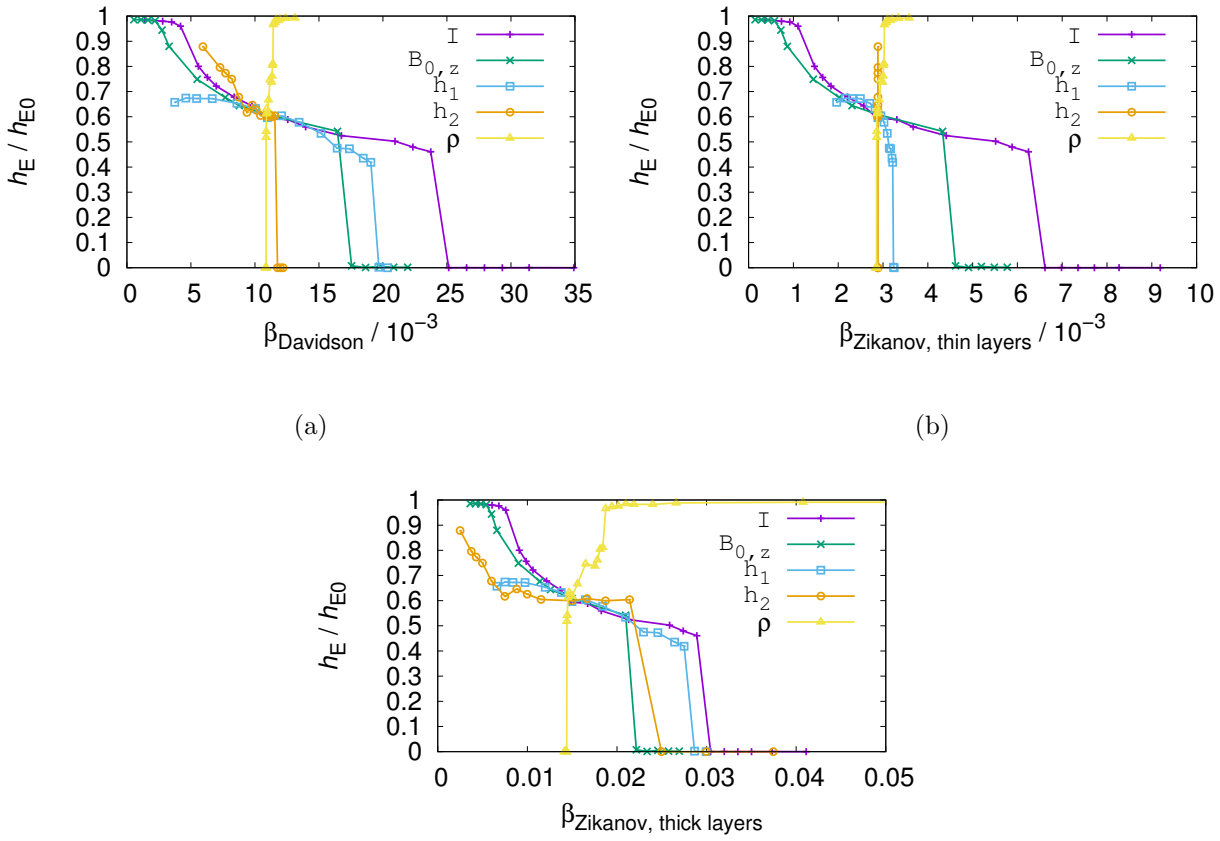

FIG. 13. Remaining minimal salt layer thickness depending on the dimensionless parameter β as deduced from Davidson and Lindsay[41] (a) and Zikanov[28] (b-c).

in LMBs – but only for our fixed aspect ratio. It is even possible to estimate the critical value for a short-circuit of the cell (for any aspect ratio). An improved dimensionless parameter should be developed for deep layers to better model the influence of the layer thicknesses. It should further include viscosity, surface tension as well as induction effects.

C. Wave equation and short-circuit

In this section we explore the shape of the interface as well as the sudden short-circuit. Figure 14a shows the minimal and maximal height of both interfaces – depending on time. We observe after 50 s a stationary sloshing; the interfaces do not touch each other. Figure 14b now illustrates the shape of the upper metal-electrolyte interface around the circumference of the cylinder. We assess here the hypothesis that this shape can be described as a solitary

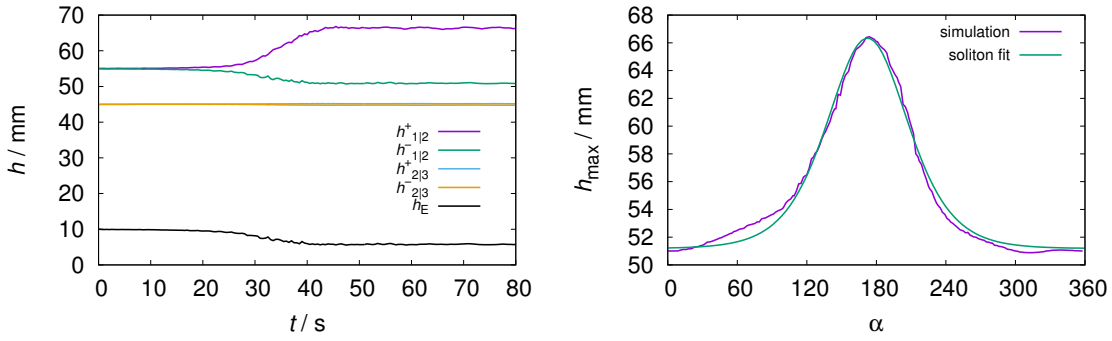

(a) (b)

FIG. 14. Temporal evolution of electrolyte layer thickness and minimal and maximal elevation of both interfaces (a) and maximal elevation of the upper interface over the circumference (b) ($I = 100\,\mathrm{A}$, $B_z = 10\,\mathrm{mT}$, $h_1 = h_3 = 4.5\,\mathrm{cm}$, $h_2 = 1\,\mathrm{cm}$).

wave[74]. Similar to the solution of the Korteweg-de-Vries equation, we describe the interface height as

$$h_I = h_0 + a\,\mathrm{sech}^2\left(kr(\alpha - \omega t)\right) \tag{36}$$

with its minimal height h_0, amplitude a and angle α. The wave number k defines the width of the crest, the angular frequency ω its speed. This equation nicely fits the observed interface shape (figure 14b); however, it allows only symmetrical crests. Especially for high currents the real wave front is very steep, but the tail quite smooth.

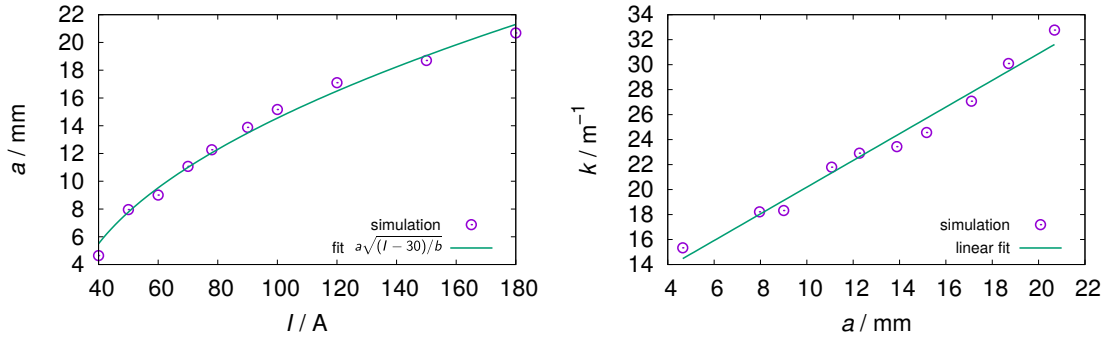

(a) (b)

FIG. 15. Amplitude of the elevation of the upper interface depending on the cell current (a) and dependence of the wave number on the amplitude of the wave (b) ($B_z = 10\,\mathrm{mT}$, $h_1 = h_3 = 4.5\,\mathrm{cm}$, $h_2 = 1\,\mathrm{cm}$).

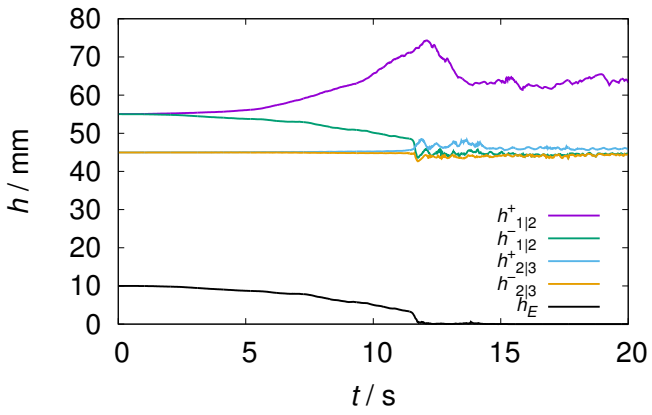

FIG. 16. Temporal evolution of electrolyte layer thickness and minimal and maximal elevation of both interfaces for $I = 200\,\mathrm{A}$ ($B_z = 10\,\mathrm{mT}$, $h_1 = h_3 = 4.5\,\mathrm{cm}$, $h_2 = 1\,\mathrm{cm}$).

In figure 15a we show the dependence of the wave amplitude a on the cell current I. As the relation between both quantities appears to be a square root curve, Ginzburg-Landau theory may apply here[75]. However, the latter is usually used to decribe weakly nonlinear regimes, while solitons are strongly nonlinear solutions.

Further, we study the relation of width and amplitude of the wave crest by comparing k and a in figure 15b. The relation is linear, which does not match well the solution of the Korteweg-de-Vries equation. Its solution usually suggests a quadratic amplitude compared to the wave number[74].

In figure 16 we show a simulation of a sloshing instability leading to a short-circuit. The trough decreases quite slowly, and short-circuits then suddenly. At the same time, the lower interface is deformed and starts to oscillate; the crest of the upper interface decreases again. This sudden interface deformation can have three reasons: surface tension, electromagnetic force or velocity. Surface tension rather dampens waves; the Lorentz force at the short-circuit will point to the cell axis and decrease pressure at the wall. Both do not provide a clear explanation of the short-circuit. We show therefore in figure 17 three different plots of the velocity on the circumference of the cell. With a rising crest, the slope of the wave front increases. This leads to a considerable flow in front of it in anti-clockwise direction (figure 17b). We assume that this flow decreases the local pressure leading to a sudden pinching of the electrolyte layer (figure 17c), maybe in concert with the locally concentrated Lorentz force. The lowered pressure may also explain the waves appearing at the lower interface.

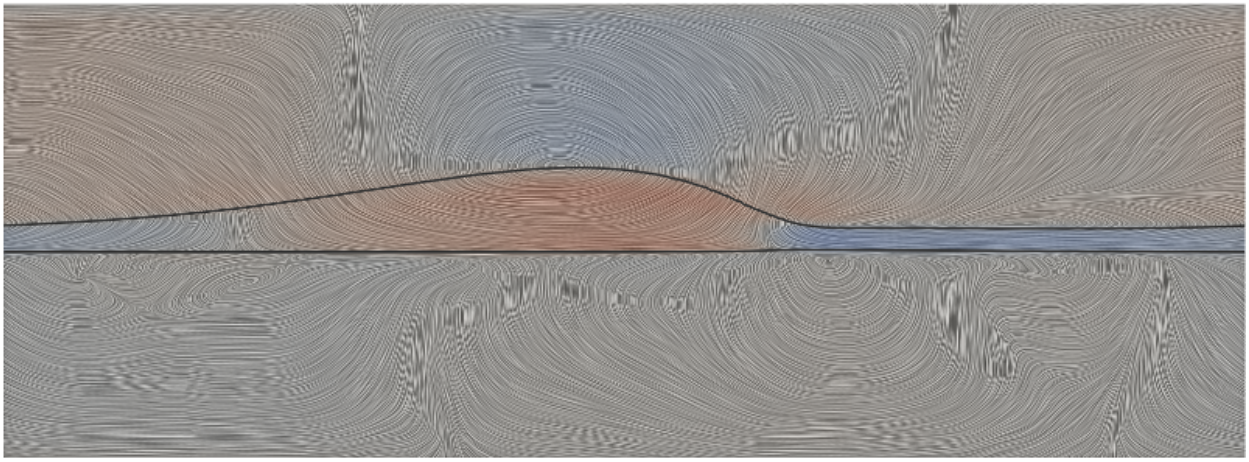

(a) $t = 10.7\,\mathrm{s}$

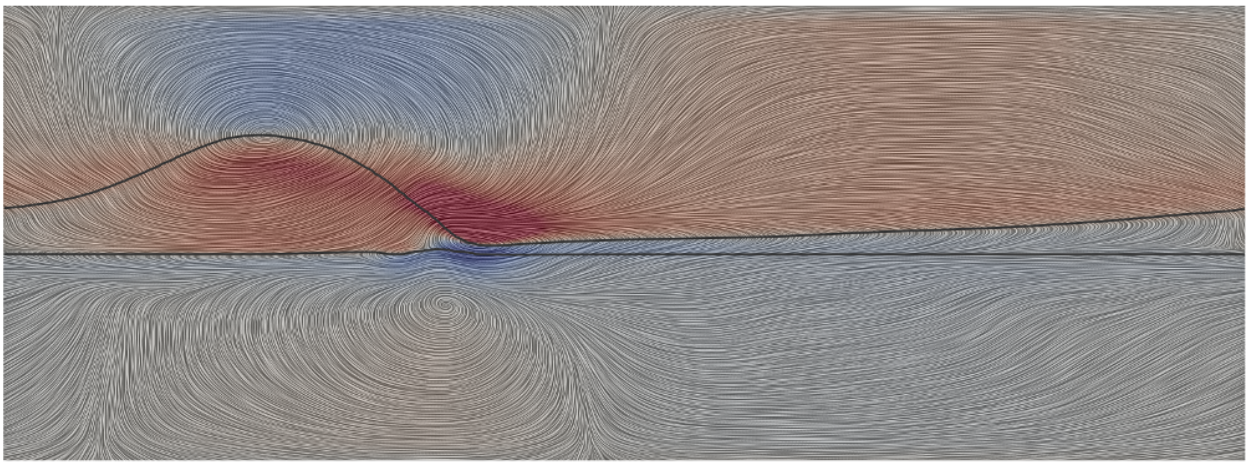

(b) $t = 12.47\,\mathrm{s}$

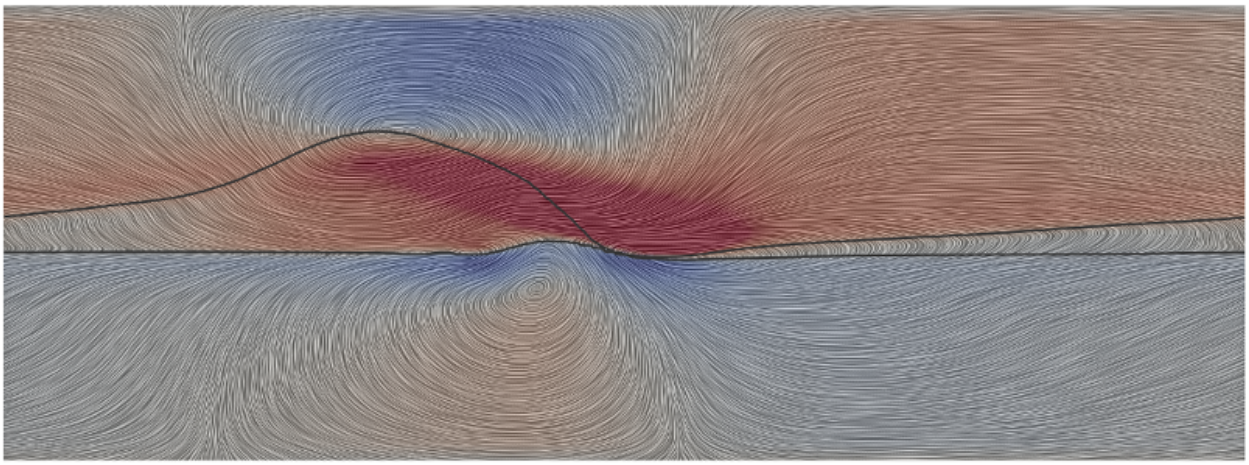

(c) $t = 12.67\,\mathrm{s}$

FIG. 17. Interface deformation, velocity and streamlines on the curved surface area of the cylinder ($I = 200\,\mathrm{A}$, $B_z = 10\,\mathrm{mT}$, $h_1 = h_3 = 4.5\,\mathrm{cm}$, $h_2 = 1\,\mathrm{cm}$). Red color indicates a positive velocity (to the right, i.e. anti-clockwise), blue color a negativ flow (to the left, i.e. clockwise).

D. Conclusion and application to real cells

Today's liquid metal batteries (LMB) are rather shallow, having a diameter in the order of 20 cm. Next generation LMBs may hopefully be considerably larger in size, with the height depending on the desired capacity of the cell. For small as for large cells, the electrolyte layer must be as thin as possible due to its high resistance. A typical value[76] is 4-10 mm. Current densities can strongly vary[76]: from 100 mA/cm^2 for energy-efficient discharge and high rate capabilities to 1 A/cm^2 for fast (dis-)charge. Li||Te and Li||Se cells even reached values of 13 A/cm^2. A realistic value of the background magnetic field can be as for aluminium reduction cells between 1 and 10 mT[38].

Using the Sele criterion

$$\beta_{\mathrm{Sele}} = \frac{Jd^2\pi b}{4g(\rho_2 - \rho_1)h_1 h_1} < \beta_{\mathrm{cr}} \tag{37}$$

and knowing the critical (Sele) parameter for the onset of sloshing $\beta = 0.35$ and the short-circuit $\beta = 2$, we can estimate whether a certain LMB will be stable, unstable or even short-circuited. The necessary physical quantities of the most common LMBs are listed in table II. Note that strictly speaking $\beta = 0.35$ for the onset of sloshing holds only for our aspect ratios ($h_1/d = 0.45$, $h_2/d = 0.1$). Only to get a first impression we *assume* β_{cr} to be the same also for shallower electrolyte layers. We show in figure 18 the onset of

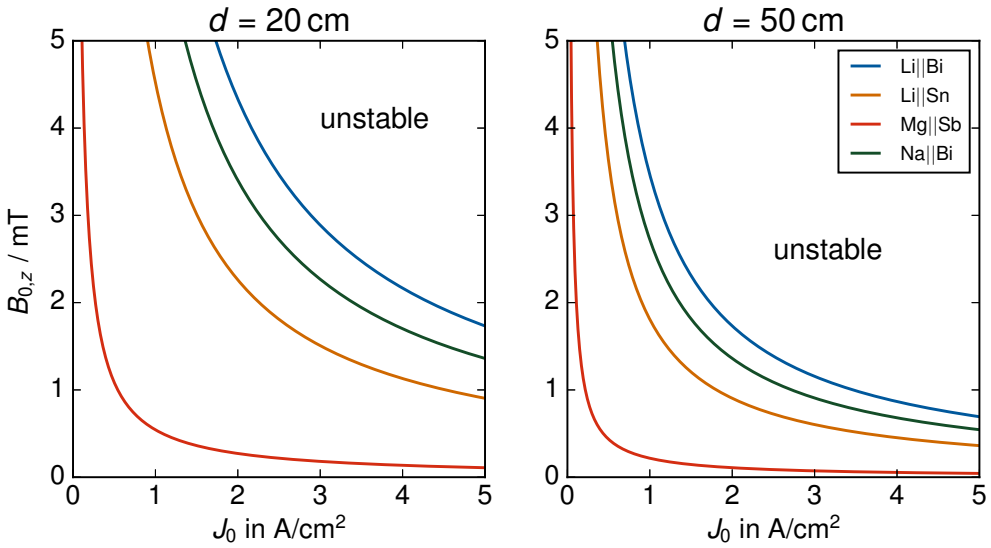

FIG. 18. Onset of sloshing ($\beta = 0.35$) depending on current density J_0 and magnetic background field $B_{0,z}$. The aspect ratio of the anode $h_1/d = 0.45$ is constant, the electrolyte layer 4 mm thick.

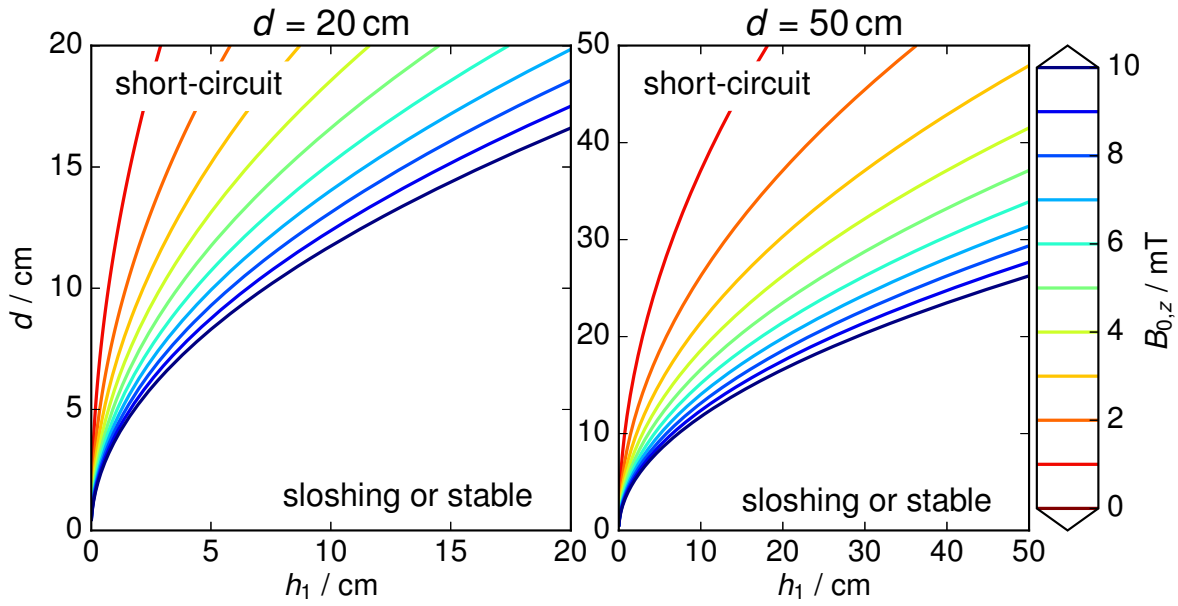

FIG. 19. Short circuit ($\beta = 2$) of an LMB depending on the height of the top metal layer h_1, the cell diameter d and magnetic field $B_{0,z}$ for a Mg||Sb cell. The height of the electrolyte layer is assumed to be 4 mm, the current density 1 A/cm^2.

sloshing depending on current density and $B_{0,z}$ for different cells of diameter 20 and 50 cm. Obviously, metal pad rolling can already set in in rather small cells with a diameter of a few decimeters. Due to its small density difference, the Mg||Sb cell is the most vulnerable one.

In figure 19 we illustrate the short-circuit of our exemplary Mg||Sb cell in dependence of $B_{0,z}$, the diameter d and upper metal height h_1. We use an electrolyte thickness of 4 mm and a current density of 1 A/cm^2. A small 10 cm Mg||Sb cell, using a 5 cm high upper metal layer can already be short-circuited by the presence of a 6 mT strong vertical background field.

IV. SUMMARY AND OUTLOOK

The main purpose of this paper was to show that the presence of a vertical magnetic field can spark the metal pad roll instability in liquid metal batteries (LMBs). This interface instability can appear in any cell as long as the current and magnetic background field are strong enough; it may finally short-circuit an LMB. In real cells (with a limited current density) the appearance of sloshing must be taken into account if the diameter is

TABLE II. Properties of liquid metal batteries: operating temperature, open circuit voltage, maximum current density and density difference upper metal-electrolyte.

cell	electrolyte	T_{op}	U_0	J_{max}	$\Delta\rho$	literature
		°C	V	A/cm^2	kg/m^3	
K||Hg	KBr-KI-KOH	250	1.1	0.1	1759	[73,77–80]
Li||Bi	LiCl-LiF-LiI	485	1.4	6.1	2202	[81–83]
Li||Pb	LiCl-LiF-LiI	483	0.6	0.4	2202	[17,83–85]
Li||Se	LiCl-LiF-LiI	375	2.4	13	2192	[9,73,83]
Li||Sn	LiCl-LiF	400	0.75	1	1149	[8,10,73,83,86]
Li||Te	LiCl-LiF-LiI	475	1.9	12.7	2201	[8,73,83,87]
Li||Zn	KCl-LiCl	486	0.64	0.3	1140	[73,83,84]
Mg||Sb	KCl-$MgCl_2$-NaCl	700	0.6	0.2	138	[13,32,73,88]
Na||Bi	NaCl-NaI-NaF	550	0.7	2.2	1729	[8,79,82]
Na||Hg	NaI-NaOH	275	0.78	0.36		[29,73,79,89]
Na||Pb	NaCl-NaF-NaI	575	0.5	0.2	1713	[79,82,84,85]
Na||Sn	NaCl-NaI	625	0.55	0.77	1554	[4,73,79,82,90]

larger than some centimeters, especially for Mg||Sb cells. Metal pad rolling can therefore be considered as one of the most important instabilities in the operation of LMBs. Yet, it can be prevented by choosing high (upper metal) layers, by an appropriate design of the bus system (minimising vertical magnetic fields) and by using a rectangular cross section instead of cylindrical or square cells.

Metal pad rolling is already well known from aluminium reduction cells. We have indentified a Sele mechanism explaining the wave propagation. The wave period is well described by the dispersion relation for gravity waves, if accounting also for surface tension. We have further studied a wide range of parameters influencing onset and intensity of sloshing: besides of strong vertical fields, also high cell currents lead to instability. Consequently, large cells are particularly vulnerable. The density difference between alkaline metal and salt should be high for stable LMBs; shallow (upper metal and electrolyte) layers promote instability. High viscosities again stabilise the cell. Many of these parameters can be combined to a dimensionless number (Sele criterion, equation 37) characterising onset and intensity of

sloshing. While the Sele criterion models well the influence of current, magnetic field and density, it partially fails describing the influence of the layer thickness of typical LMBs.

Increasing e.g. the cell current, the electrolytes minimal thickness decreases (figure 5). We have proposed to describe the influence of several parameters on this salt layer thickness by Ginzburg-Landau theory. For small and moderate deformation of the electrolyte layer, we suggest to describe the shape of the upper metal-electrolyte interface as some kind of solitary wave. The sudden short-circuit of the salt layer is attributed to a strong flow in front of the wave crest.

Our simulation can only give a first rough overview on the sloshing instability in LMBs. Maybe the most important step would be an experimental evidence of the instability in a three layer system. Although metal pad rolling was intensively studied in (the two-layer layer system of) aluminium reduction cells, the dimenionless parameter defining its onset is imperfect. Most importantly, the Sele criterion should be extended to cells of high aspect ratio to describe the influence of the layer heights better. It could further be complemented by the influence of induction, surface tension and viscosity and maybe adapted to our three layer system. The very sudden short-circuit will need further and more detailed studies. For this purpose it may be necessary to improve the mixture model for conductivity as well as the implementation of surface tension in our solver. A comparison of the OpenFOAM solver with the spectral code SFEMaNS[91] is planned.

ACKNOWLEDGMENTS

This work was supported by Helmholtz-Gemeinschaft Deutscher Forschungszentren (HGF) in frame of the Helmholtz Alliance “Liquid metal technologies” (LIMTECH). The computations were performed on the Bull HPC-Cluster “Taurus” at the Center for Information Services and High Performance Computing (ZIH) at TU Dresden and on the cluster “Hydra” at Helmholtz-Zentrum Dresden – Rossendorf. Fruitful discussions with Valdis Bojarevics, Douglas Kelley, Cornel Lalau, Steffen Landgraf, Michael Nimtz, Marco Starace and Oleg Zikanov on several aspects of metal pad roll instability and liquid metal batteries are gratefully acknowledged. N. Weber thanks Henrik Schulz for the HPC support.

REFERENCES

[1]M. S. Wittingham, "History, Evolution, and Future Status of Energy Storage," Proc. IEEE **100**, 1518–1534 (2012).

[2]P. H. J. Nardelli, N. Rubido, C. Wang, M. S. Baptista, C. Pomalaza-Raez, P. Cardieri, and M. Latva-aho, "Models for the modern power grid," Eur. Phys. J. Spec. Top. **223**, 2423–2437 (2014).

[3]B. Agruss and H. R. Karas, "The Thermally Regenerative Liquid Metal Concentration Cell," in *Regenerative EMF Cells*, Advances in Chemistry, Vol. 64, edited by R. F. Gold (American Chemical Society, Washington, D.C., 1967) pp. 62–81.

[4]R. D. Weaver, S. W. Smith, and N. L. Willmann, "The Sodium-Tin Liquid-Metal Cell," J. Electrochem. Soc. **109**, 653–657 (1962).

[5]B. Agruss, "The Thermally Regenerative Liquid-Metal Cell," J. Electrochem. Soc. **110**, 1097–1103 (1963).

[6]R. K. Steunenberg and L. Burris, "From Test Tube to Pilot Plant: A 50 Year History of the Chemical Technology Division at Argonne National Laboratory," Tech. Rep. ANL-00/16 (Argonne National Laboratory, 2000).

[7]C. E. Crouthamel and H. L. Recht, eds., *Regenerative EMF Cells*, Vol. 64 (American Chemical Society, 1967).

[8]E. J. Cairns, C. E. Crouthamel, A. K. Fischer, M. S. Foster, J. C. Hesson, C. E. Johnson, H. Shimotake, and A. D. Tevebaugh, *Galvanic Cells with Fused-Salt Electrolytes*, ANL-7316 (Argonne National Laboratory, 1967).

[9]E. J. Cairns and H. Shimotake, "High-Temperature Batteries," Science **164**, 1347–1355 (1969).

[10]D. A. J. Swinkels, "Molten Salt Batteries and Fuel Cells," in *Advances in Molten Salt Chemistry*, Vol. 1, edited by J. Braunstein, G. Mamantov, and G. P. Smith (Plenum Press, New York, 1971) pp. 165–223.

[11]H. Kim, D. A. Boysen, J. M. Newhouse, B. L. Spatocco, B. Chung, P. J. Burke, D. J. Bradwell, K. Jiang, A. A. Tomaszowska, K. Wang, W. Wei, L. A. Ortiz, S. A. Barriga, S. M. Poizeau, and D. R. Sadoway, "Liquid Metal Batteries: Past, Present, and Future," Chem. Rev. **113**, 2075–2099 (2013).

[12]B. L. Spatocco and D. R. Sadoway, "Cost-Based Discovery for Engineering Solutions," in *Electrochemical Engineering Across Scales: From Molecules to Processes*, Advances in Electrochemical Science and Engineering, Vol. 15, edited by R. C. Alkire, P. N. Bartlett, and J. Lipkowski (Wiley-VCH, 2015) pp. 227–262.

[13]D. J. Bradwell, H. Kim, A. H. C. Sirk, and D. R. Sadoway, "Magnesium–Antimony Liquid Metal Battery for Stationary Energy Storage," J. Am. Chem. Soc. **134**, 1895–1897 (2012).

[14]H. Kim, D. A. Boysen, T. Ouchi, and D. R. Sadoway, "Calcium - bismuth electrodes for large - scale energy storage," J. Power Sources **241**, 239–248 (2013).

[15]T. Ouchi, H. Kim, X. Ning, and D. R. Sadoway, "Calcium-Antimony Alloys as Electrodes for Liquid Metal Batteries," J. Electrochem. Soc. **161**, A1898–A1904 (2014).

[16]T. Ouchi, H. Kim, B. L. Spatocco, and D. R. Sadoway, "Calcium-based multi-element chemistry for grid-scale electrochemical energy storage," Nat. Commun. **7**, 10999 (2016).

[17]K. Wang, K. Jiang, B. Chung, T. Ouchi, P. J. Burke, D. A. Boysen, D. J. Bradwell, H. Kim, U. Muecke, and D. R. Sadoway, "Lithium–antimony–lead liquid metal battery for grid-level energy storage," Nature **514**, 348–350 (2014).

[18]B. L. Spatocco, T. Ouchi, G. Lambotte, P. J. Burke, and D. R. Sadoway, "Low-Temperature Molten Salt Electrolytes for Membrane-Free Sodium Metal Batteries," J. Electrochem. Soc. **162**, A2729–A2736 (2015).

[19]F. Stefani, T. Weier, T. Gundrum, and G. Gerbeth, "How to circumvent the size limitation of liquid metal batteries due to the Tayler instability," Energy Convers. Manag. **52**, 2982 – 2986 (2011).

[20]N. Weber, V. Galindo, F. Stefani, and T. Weier, "Current-driven flow instabilities in large-scale liquid metal batteries, and how to tame them," J. Power Sources **265**, 166–173 (2014).

[21]W. Herreman, C. Nore, L. Cappanera, and J.-L. Guermond, "Tayler instability in liquid metal columns and liquid metal batteries," J. Fluid Mech. **771**, 79–114 (2015).

[22]Y. Shen and O. Zikanov, "Thermal convection in a liquid metal battery," Theor. Comput. Fluid Dyn. **30**, 275–294 (2016).

[23]A. Perez and D. H. Kelley, "Ultrasound Velocity Measurement in a Liquid Metal Electrode," J. Vis. Exp. (2015).

[24]A. Beltrán, "MHD natural convection flow in a liquid metal electrode," Appl. Therm. Eng. (2016).

[25]D. H. Kelley and D. R. Sadoway, "Mixing in a liquid metal electrode," Phys. Fluids **26**, 057102 (2014).

[26]N. Weber, V. Galindo, J. Priede, F. Stefani, and T. Weier, "The influence of current collectors on Tayler instability and electro vortex flows in liquid metal batteries," Phys. Fluids **27** (2015).

[27]F. Stefani, V. Galindo, C. Kasprzyk, S. Landgraf, M. Seilmayer, M. Starace, N. Weber, and T. Weier, "Magnetohydrodynamic effects in liquid metal batteries," IOP Conf. Ser. Mater. Sci. Eng. **143**, 012024 (2016).

[28]O. Zikanov, "Metal pad instabilities in liquid metal batteries," Phys. Rev. E **92** (2015).

[29]L. A. Herédy, M. L. Iverson, G. D. Ulrich, and H. L. Recht, "Development of a thermally regenerative Sodium-Mercury galvanic system Part I Electrochemical and Chemical Behavior of Sodium-Mercury Galvanic Cells," in *Regenerative EMF Cells* (1967) pp. 30–42.

[30]H. Shimotake and E. J. Cairns, "Bimetallic galvanic cells with fused-salt electrolytes," in *Advances in Energy Conversion Engineering* (ASME, Florida, 1967) pp. 951–962.

[31]H. Kim, D. A. Boysen, D. J. Bradwell, B. Chung, K. Jiang, A. A. Tomaszowska, K. Wang, W. Wei, and D. R. Sadoway, "Thermodynamic properties of calcium–bismuth alloys determined by emf measurements," Electrochimica Acta **60**, 154–162 (2012).

[32]D. J. Bradwell, *Liquid Metal Batteries: Ambipolar Electrolysis and Alkaline Earth Electroalloying Cells*, Ph.D. thesis, Massachusetts Institute of Technology (2011).

[33]D. Sadoway, G. Ceder, and D. Bradwell, "High-amperage energy storage device with liquid metal negativ electrode and methods," (2012), US Patent 8,268,471 B2.

[34]R. E. Huggins, *Energy Storage* (Springer, 2016).

[35]J. W. Evans and D. P. Ziegler, "The Electrolytic Production of Aluminum," in *Electrochemical Engineering*, Encyclopedia of Electrochemistry, Vol. 5, edited by A. Bard and M. Startmann (Wiley-VCH, Weinheim, 2007) pp. 224–265, volume editors: Macdonald, D.D. and Schmuki, P.

[36]J.-F. Gerbeau, C. Le Bris, and T. Lelièvre, *Mathematical Methods for the Magnetohydrodynamics of Liquid Metals*, Numerical mathematics and scientific computation (Oxford University Press, Oxford ; New York, 2006).

[37]P. A. Davidson, "Overcoming instabilities in aluminium reduction cells: A route to cheaper aluminium," Mater. Sci. Technol. **16**, 475–479 (2000).

[38]S. Molokov, G. El, and A. Lukyanov, "Classification of instability modes in a model of aluminium reduction cells with a uniform magnetic field," Theor. Comput. Fluid Dyn. **25**, 261–279 (2011).

[39]A. Pedchenko, S. Molokov, J. Priede, A. Lukyanov, and P. J. Thomas, "Experimental model of the interfacial instability in aluminium reduction cells," Eur. Lett **88**, 24001 (2009).

[40]T. Sele, "Instabilities of the metal surface in electrolytic alumina reduction cells," Metall. Mater. Trans. B **8**, 613–618 (1977).

[41]P. A. Davidson and R. I. Lindsay, "Stability of interfacial waves in aluminium reduction cells," J. Fluid Mech. **362**, 273–295 (1998).

[42]D. Munger, *Stabiliié Magnétohydrodynamique Des Cuves D'électrolyse: Aspects Physiques et Idées Nouvelles*, Ph.D. thesis, Université de Montréal (2008).

[43]N. Weber, P. Beckstein, V. Galindo, F. Stefani, T. Weier, W. Herreman, and C. Nore, "Metal pad roll instability in liquid metal batteries," in *Proceedings of the 10th PAMIR International Conference* (2016).

[44]N. Urata, "Magnetics and metal pad instability," Light Met. , 581–591 (1985).

[45]V. Bojarevics and M. V. Romerio, "Long waves instability of liquid metal-electrolyte interface in aluminium electrolysis cell: A generalization of Sele's criterion," Eur. J. Mech. - BFluids **13**, 33–56 (1994).

[46]A. D. Sneyd, "Interfacial instabilities in aluminium reduction cells," J. Fluid Mech. **236**, 111–126 (1992).

[47]A. D. Sneyd and A. Wang, "Interfacial instability due to MHD mode coupling in aluminium reduction cells," J. Fluid Mech. **263**, 343–359 (1994).

[48]M. Segatz and C. Droste, "Analysis of magnetohydrodynamic instabilities in aluminium reduction cells," Light Met. , 313–322 (1994).

[49]A. Lukyanov, G. El, and S. Molokov, "Instability of MHD-modified interfacial gravity waves revisited," Phys. Lett. A **290**, 165–172 (2001).

[50]R. Moreau and D. Ziegler, "Stability of aluminum cells: A new approach," Light Met. , 359–364 (1986).

[51]F. Moisy, O. Doar, T. Pasutto, O. Daube, and M. Rabaud, "Experimental and numerical study of the shear layer instability between two counter-rotating disks," J. Fluid Mech. **507**, 175–202 (2004).

[52]C. Nore, M. Tartar, O. Daube, and L. S. Tuckerman, "Survey of instability thresholds of flow between exactly counter-rotating disks," J. Fluid Mech. **511**, 45–65 (2004).

[53]V. Bojarevics, K. Pericleous, and others, "Comparison of MHD models for aluminium reduction cells," Proc. TMS Light Met. , 347–352 (2006).

[54]V. Bojarevics, "Non-linear waves with electromagnetic interaction in aluminium electrolysis cells," Prog. Astronaut. Aeronaut. (1998).

[55]O. Zikanov, A. Thess, P. A. Davidson, and D. P. Ziegler, "A new approach to numerical simulation of melt flows and interface instability in Hall-Heroult cells," Metall. Mater. Trans. B **31**, 1541–1550 (2000).

[56]M. Flueck, A. Janka, C. Laurent, M. Picasso, J. Rappaz, and G. Steiner, "Some Mathematical and Numerical Aspects in Aluminum Production," J. Sci. Comput. **43**, 313–325 (2010).

[57]M. C. Dube, "Extraction and refining of aluminium," in *Proc. Symp. Non-Ferrous Metal Industry in India*, edited by B. Nijhawan and A. Chatterjee (National Metallurgical Laboratory, Jamshedpur, India, 1954) pp. 127 – 138.

[58]S. J. Lindsay, "Very High Purity Aluminum: An Historical Perspective," JOM **66**, 217–222 (2014).

[59]A. D. Sneyd, "Stability of fluid layers carrying a normal electric current," J. Fluid Mech. **156**, 223–236 (1985).

[60]J. Descloux, M. Flueck, and M. Romerio, "Stability in aluminium reduction cells: A spectral problem solved by an iterative procedure," Light Met. , 275–281 (1994).

[61]J. Descloux, M. Flueck, and M. V. Romerio, "Modelling for instabilities in Hall–Heroult cells: Mathematical and numerical aspects," in *Magnetohydrodynamics in Process Metallurgy*, edited by J. Szekely and J. W. Evans (1991) pp. 107–110.

[62]N. Weber, V. Galindo, F. Stefani, T. Weier, and T. Wondrak, "Numerical simulation of the Tayler instability in liquid metals," New J. Phys. **15** (2013).

[63]O. Ubbink, *Numerical Prediction of Two Fluid Systems with Sharp Interfaces*, Ph.D. thesis, University of London (1997).

[64]H. Rusche, *Computational Fluid Dynamics of Dispersed Two-Phase Flows at High Phase Fractions*, Ph.D. thesis, Imperial College London (2002).

[65]S. S. Deshpande, L. Anumolu, and M. F. Trujillo, "Evaluating the performance of the two-phase flow solver interFoam," Comput. Sci. Discov. **5**, 014016 (2012).

[66]N. Weber, V. Galindo, F. Stefani, and T. Weier, "The Tayler instability at low magnetic Prandtl numbers: Between chiral symmetry breaking and helicity oscillations," New J. Phys. **17**, 113013 (2015).

[67]V. Bandaru, T. Boeck, D. Krasnov, and J. Schumacher, "A hybrid finite difference–boundary element procedure for the simulation of turbulent MHD duct flow at finite magnetic Reynolds number," J. Comput. Phys. **304**, 320–339 (2016).

[68]L. A. Santalo, *Vectores Y Tensores Con Sus Aplicaciones* (Buenos Aires, 1993).

[69]J. K. Carson, S. J. Lovatt, D. J. Tanner, and A. C. Cleland, "Thermal conductivity bounds for isotropic, porous materials," Int. J. Heat Mass Transf. **48**, 2150–2158 (2005).

[70]J. U. Brackbill, D. B. Kothe, and C. Zemach, "A continuum method for modeling surface tension," J. Comput. Phys. **100**, 335–354 (1992).

[71]J. N. Israelachvili, *Intermolecular and Surface Forces*, 3rd ed. (Academic Press, Burlington, MA, 2011).

[72]N. E. Todreas and P. Hejzlar, "Flexible Conversion Ratio Fast Reactor Systems Evaluation," Tech. Rep. (MIT, 2008).

[73]C. J. Smithells, W. F. Gale, and T. C. Totemeier, *Smithells Metals Reference Book*, 8th ed. (Elsevier Butterworth-Heinemann, Amsterdam ; Boston, 2004).

[74]L. Munteanu and S. Donescu, *Introduction to Soliton Theory: Applications to Mechanics* (Kluwer Academic Publishers, Dordrecht; Boston, 2004).

[75]I. S. Aranson and L. Kramer, "The world of the complex Ginzburg-Landau equation," Rev. Mod. Phys. **74**, 99–143 (2002).

[76]N. Weber, *Modellierung von Tayler-Instabilität und Elektrowirbelströmungen in Flüssigmetallbatterien*, Ph.D. thesis, Technische Universität Dresden (2016).

[77]B. Agruss and H. R. Karas, "First Quarterly Technical Progress Report on Design and Development of a Liquid Metal Cell for the Period 1 January 1962 – 31 March 1962," Tech. Rep. (Armed Service Technical Information Agency, 1962).

[78]H. L. Chum and R. A. Osteryoung, *Review of Thermally Regenerative Electrochemical Systems* (Solar Energy Research Institute, 1980).

[79]International Atomic Energy Agency, *Thermophysical Properties of Materials for Nuclear Engineering: A Tutorial and Collection of Data.* (International Atomic Energy Agency, Vienna, 2008).

[80]H. R. Karas and J. D. Mangus, *First Quarterly Technical Progress Report on Research and Development of an Advanced Laboratory Liquid Metal Regenerative Fuel Cell for the Period 1 March – 18 March 1963*, Vol. AD 405 481 (Defence Documentation Center, 1963).

[81]H. Shimotake, G. L. Rogers, and E. J. Cairns, "Secondary Cells with Lithium Anodes and Immobilized Fused-Salt Electrolytes," Ind. Eng. Chem. Process Des. Dev. **8**, 51–56 (1969).

[82]V. Sobolev, *Database of Thermophysical Properties of Liquid Metal Coolants for GEN-IV* (SCK CEN, 2010).

[83]S. J. Zinkle, "Summary of Physical Properties for Lithium, Pb-17Li, and (LiF)n•BeF2 Coolants," in *APEX Study Meeting* (1998).

[84]H. L. Chum and R. A. Osteryoung, *Review of Thermally Regenerative Electrochemical Cells* (Solar Energy Research Institute, 1981).

[85]V. Sobolev, "Thermophysical properties of lead and lead–bismuth eutectic," J. Nucl. Mater. **362**, 235–247 (2007).

[86]R. N. Lyon, ed., *Liquid-Metals Handbook* (Oak Ridge National Laboratory, 1954).

[87]E. J. Cairns and H. Shimotake, "Recent advances in fuel cells and their application to new hybrid systems," Adv. Chem. **90**, 321–350 (1969).

[88]F. Aqra and A. Ayyad, "Theoretical Estimation of Temperature-Dependent Surface Tension of Liquid Antimony, Boron, and Sulfur," Metall. Mater. Trans. B **42**, 437–440 (2011).

[89]B. L. Spatocco, P. J. Burke, and D. R. Sadoway, "Low temperature liquid metal batteries for grid-scaled storage," (2014), US Patent Nr. 0099522 A1.

[90]G. J. Janz, R. P. T. Tomkins, and C. B. Allen, "Molten Salts: Volume 4, Part 4 Mixed Halide Melts Electrical Conductance, Density, Viscosity, and Surface Tension Data," J. Phys. Chem. Ref. Data **8**, 125 (1979).

[91]J.-L. Guermond, R. Laguerre, J. Léorat, and C. Nore, "Nonlinear magnetohydrodynamics in axisymmetric heterogeneous domains using a Fourier/finite element technique and an interior penalty method," J. Comput. Phys. **228**, 2739–2757 (2009).

Appendix A: Numerical model

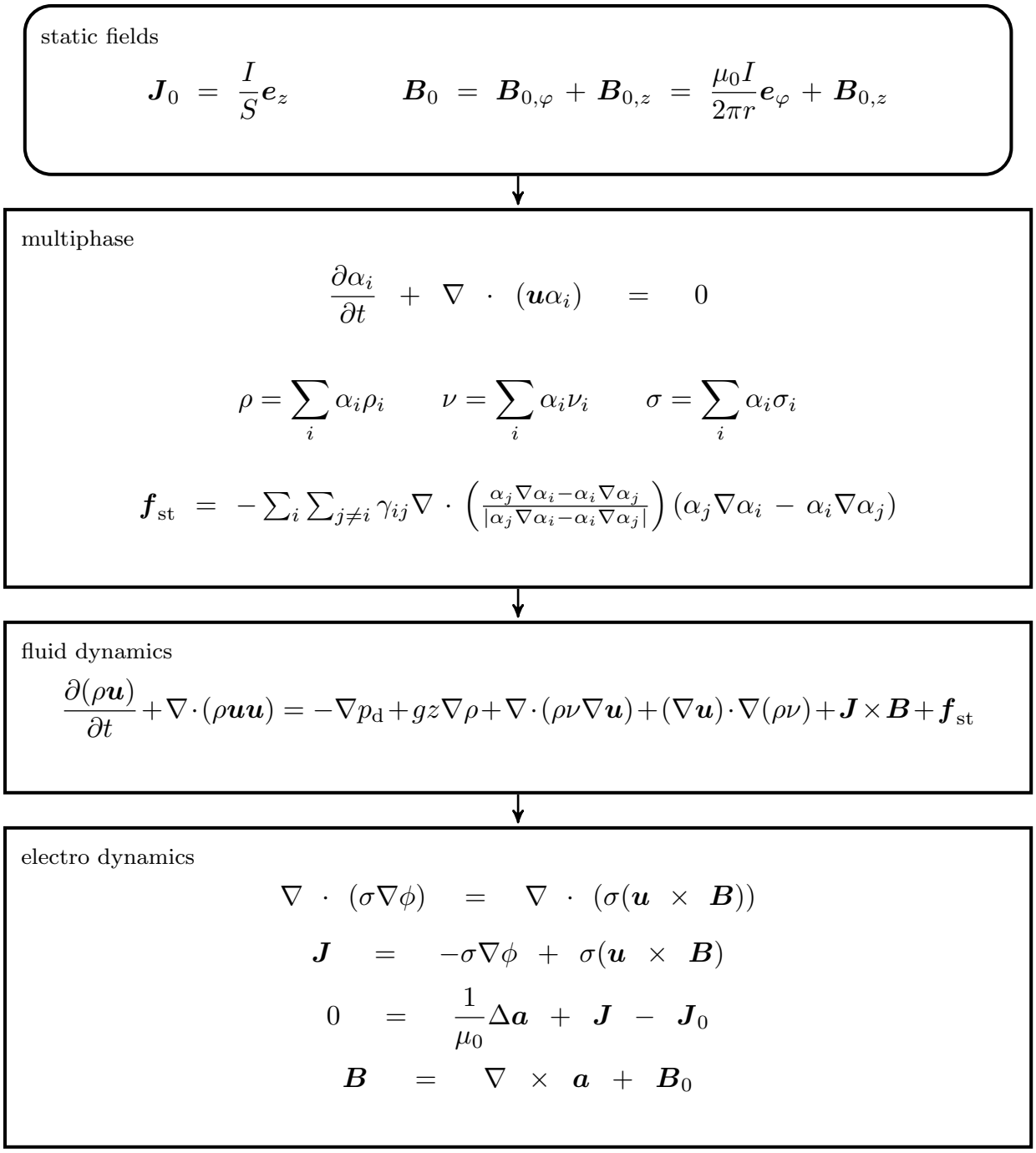

FIG. 20. Flowchart for multiphase simulation.